Electronic Structure and Magnetism of Pristine, Defected, and Strained Ti_2N MXene

Yogendra Limbu[1], Gopi Chandra Kaphle[1],* Alok Lal Karn[1],
Niraj Kumar Shah[1], Hari Paudyal[2], and Durga Paudyal[3,4]
[1] *Central Department of Physics, Tribhuvan University, Kirtipur, Kathmandu, Nepal*
[2] *Department of Physics, Applied Physics, and Astronomy, Binghamton University-SUNY, Binghamton, New York 13902, USA*
[3] *Ames Laboratory of the US DOE, Iowa State University, Ames, IA 50011, USA and*
[4] *Department of Electrical and Computer Engineering, Iowa State University, Ames, IA 50011, USA*

From first principles electronic structure calculations, we unravel the evolution of structural, electronic, and magnetic properties of pristine, defected, and strained titanium nitride MXene with different functional groups (-F, -O, -H, and -OH). The formation and cohesive energies reveal their chemical stability. The dynamical stability of Ti_2N mono-layer is also confirmed by phonon calculations. The MAX phase and defect free functionalized MXenes are metallic except for oxygen terminated (Ti_2NO_2) one which is 100% spin polarized half-metallic ferromagnet. The spin-orbit coupling significantly influences the bare MXene (Ti_2N) to exhibit Dirac topology and band inversion near the high symmetry directions. The strain effect sways the Fermi level thereby shifting it toward lower energy state under compression and toward higher energy state under tensile strain in Ti_2NH_2. The Ti_2NO_2 exhibits exotic electronic structure not only in pristine but also in strained and defected structures. Its half-metallic nature changes to semi-metallic under 1% compression and it is completely destroyed under 2% compression. In single vacancy defect, its band structure remarkably transforms from half-metallic to semi-conducting with large band gap in 12.5% Ti, weakly semi-conducting in 5.5% Ti, and semi-metallic in 12.5% O. The 25% N defect changes it's half-metallic characteristic to metallic. Further, the 12.5% Co substitution preserves it's half-metallic character, whereas Mn substitution allows it to convert half-metallic characteristic into weak semi-metallic characteristic preserving ferromagnetism. However, Cr substitution converts half-metallic ferromagnetic state to half-metallic anti-ferromagnetic state. The understanding made here on collective structural stability, and electronic band structure, and magnetic phenomena in novel 2D Ti_2N derived MXenes open up their possibility in designing them for synthesis.

KEYWORDS: *Structural Stability, Electronic Structure, Magnetic Phenomena, Strain, and Defect*

INTRODUCTION

After the discovery of graphene by the group of Novoselov and Geim in 2004 [1], many researchers are focusing on two-dimensional (2D) materials with diverse physical phenomena [2, 3]. Atomically-thin 2D materials have unique physical, chemical, electronic, and optical properties [4]. Graphene is limited to just carbon atoms in its composition, whereas the rapidly growing area of 2D materials include large set of transition metal (TM) carbides and nitrides (MXenes) [5]. These materials have wide range of applications in diverse field such as energy storage, water electrolyzers, super-capacitors, lithium ion batteries [6], biomedical applications [7], sensors [8], catalysts [9], and spintronic devices [10].

In 2011, a new group of 2D materials based on TM carbides were synthesized [11]. These 2D MXenes (FIG. 1b and 1c) are obtained from leaching A atoms from 3D MAX phase (FIG. 1a) with general chemical formula $M_{n+1}AX_n$ where n = 1 to 3, M is TM, A is an A-group (basically IIIA and IVA or group 13 and 14) element, and X is either carbon or nitrogen. The unit cell of the MAX phase is characterized by near close-packed M layers interleaved with the layers of a pure A-group elements and with the X atoms filling the octahedral sites[12, 13]. The 2D MXenes offer a large variety of chemical compositions compared to graphene [14]. MXenes can be thought of as conductive clays in which cation intercalation and exchange easily occur [15]. Among all experimentally synthesized and theoretically predicted MXenes, the carbide based MXenes are widely studied especially $Ti_3C_2T_2$ (T= surface termination) [16]. The synthesis of titanium nitride based MXene is quite difficult due to large value of formation energy in their 3D MAX phase and its poor stability in etchant, typically in hydrofluoric acid (HF) [17]. The Ti_4N_3 MXene was successfully synthesized from precursor Ti_4AlN_3 using molten fluoride salt to etching Al elements [18], whereas the Ti_2N MXene was synthesized with functionalized fluoride by immersing Ti_2AlN in a mixture of potassium fluoride (KF) and hydrochloric acid (HCl) [17]. Here, the surface terminated mono-layer improves the structural stability thereby changing the electronic and magnetic properties as compared to the bare MXene [19]. The nitride MXenes exhibit better pseudocapacitive performance than carbide based MXenes [20]. This type of 2D materials have high value of electrical conductivity and wide range of absorption applications, which are key to their success

in the aforementioned applications [21].

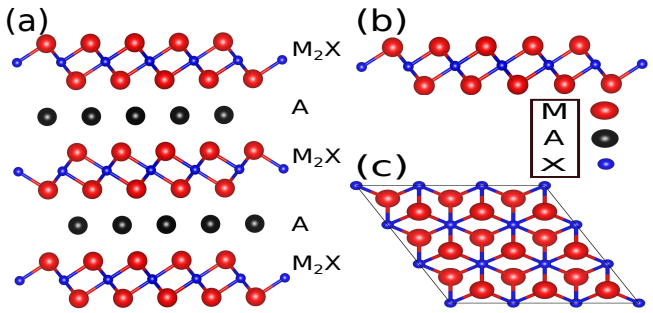

FIG. 1. (Color online) (a) Hexagonal closed packed structure of MAX phase M_2AX, and (b) and (c) are corresponding side and top views of MXene M_2X in $3 \times 3 \times 1$ super-cell.

The 2D materials are highly flexible and extremely sensitive to the applied strain to modulate electronic band structure [22–24]. The nature of band structure changes from indirect band gap to direct band gap under tensile strain and the band gap closes under compressive strain in Ti_2CO_2 MXene [25]. Despite having all fascinating properties, the defect in MXenes severely alter the structural stability, electronic, and magnetic properties [26]. The presence of intrinsic Ti defects in $Ti_3C_2T_2$ layers was experimentally determined (using scanning tunneling microscopy) in Ref. [27]. However, the detail explanation of structural defect in MXene is missing, which is addressed here.

Beside the major astonishing properties and applications of MXenes, there was a limitation in the field of storage capacity. This was solved by doping nitrogen atom in Nb_2CT_2 MXenes [28]. The Nb doping can change electronic properties by shifting the Fermi level towards the conduction band that enhances the electronic conductivity in $Ti_3C_2T_2$ [29]. Further, the B doping in oxygen terminated Ti_2C MXene improves the elastic properties with reasonably high critical strain making suitable for the flexible device applications [30].

Furthermore, the realization of free-standing single atomic layers of graphene opened a new route towards the topological phenomena in 2D materials [31–34]. The coexistence of electron and hole pockets with Dirac cone is responsible for quantum oscillation in 3D topological materials [35]. Similarly, the Zr_2Si also exhibits anisotropic Dirac cones [36]. Theoretically, the titanium carbide based MXenes can also be predicted to exhibit the Dirac topology in their electronic band structure [37]. In the similar vein, the topological and associated properties are expected in the Ti_2N MXene.

In this paper, we have studied the electronic and magnetic properties of the MAX phase, and bare and its corresponding functionalized MXenes. The chemical stability of all MXenes and MAX phase are studied with the help of cohesive and formation energies. The -O terminated MXene is relatively stable as compared to all other MXenes. The MAX phase and functionalized MXenes exhibit the non-magnetic (NM) metallicity except for O terminated one, which is predicted to be a half-metallic ferromagnet. The strain effect influences the position of the Fermi level with different topological nature. The defect in Ti_2NO_2 brings significant changes in the electronic structure and properties. The electronic properties of Ti defect strongly depend upon vacancy concentration. The half-metallic nature changes to strong and weak semiconductor depending upon the concentration. Similarly, the half-metallic property changes to semi-metallic and also remains metallic with band crossing depending on different defects. Interestingly, the TM substitution introduces peculiar magnetic to semi-metallic phenomena in Ti_2NO_2 MXene. To the best of our knowledge, the electronic band structure, effect of SOC, vacancy concentration dependent semi-conducting nature, doping, and detail explanation of half-metalicity are the new finding of this work.

THEORETICAL BACKGROUND, COMPUTATIONAL DETAILS, AND EXPERIMENTAL INFORMATION

This study uses density functional theory (DFT) in conjunction with pseudo-potential plane wave method (Quantum ESPRESSO) [38, 39]. Both Perdew-Burke-Ernzerhof (PBE) [40] and hybrid (HSE06) functionals predict very similar crystal and electronic structures of Ti_2N and related materials [19]. We also performed the HSE06 calculations to validate the results obtained from PBE particularly in Ti_2NO_2. Following this, we have used only PBE functional to describe exchange-correlation potential within the generalized gradient approximation [41], where scalar relativistic pseudo-potential for collinear calculations and fully-relativistic pseudo-potential for non-collinear calculations are considered and focused on underlying physics involved in these materials.

We have performed non-collinear calculations to study the effect of spin-orbit coupling (SOC) in the electronic band structure employing relativistic DFT [42] based on fully-relativistic pseudo-potential [43, 44]. This pseudo-potential is constructed from the solutions of Dirac type Kohn-Sham equation for four components of pseudo wave functions. The four component spinors Dirac equation changes to two components spinors Pauli-type equation when small components of the pseudo wave functions are neglected without affecting the results. Under the Pauli-type formalism, the calculated relativistic frozen-core energy implicitly includes the spin-orbit effect [45, 46].

The projected augmented wave method is used to describe the ion-electron interaction [47], with $1s^1$, $2s^2\ 2p^3$, $2s^2\ 2p^4$, $2s^2\ 2p^5$, $3s^2\ 3p^1$, and $4s^2\ 3d^2$ treated as valence electrons for H, N, O, F, Al, and Ti, respectively. A plane wave basis set with a sufficient cutoff energy of 680 eV has been used to represent valence electrons and 6800 eV

for charge density, which are sufficient for these class of materials [19].

To model 2D-lattices, we performed electronic structure calculations for bare and terminated species of 1 × 1 × 1, 2 × 2 × 1, and 3 × 3 × 1 cells. The underlying structural optimization is performed using small k-points grid of 4 × 4 × 1 with the energy convergence criterion in the order of 10^{-5} eV / cell. The geometries of MXenes were relaxed until force becomes less than or equal to 0.01 eV / Å. After full structural optimization, a large vacuum space more than 17 Å along the lattice vector c was set to avoid any interaction between MXene sheets. A densed k-points grid of 20 × 20 × 1 was used for self-consistent calculations (scf) and 25 × 25 × 1 for density of states (DOS) calculations. DOS was calculated by using Gaussian smearing method, however, the tetrahedron integration method has been used to clearly identify the half-metallic nature in Ti_2NO_2. To clearly identify the underlying band crossings, we have used a large number of energy points (2000) along high symmetry directions in band structure calculations. The dynamical matrices were calculated within density-functional perturbation theory on the irreducible set of 6 × 6 ×1 **q**-mesh.

In addition, the band structure of primitive cell is recovered from the complex band structure of super-cell by unfolding the super-cell Brillouin zone into Brillouin zone by using the bandUP (unfold.x code) computer program [48, 49] within the same exchange-correlation functional, which is based on the evaluation of spectral weight,

$$P_{m\vec{K}}(\vec{k}) = \sum_{n} |\langle \psi^{SC}_{m\vec{K}} | \psi^{PC}_{n\vec{k}} \rangle|^2$$

where $\psi^{SC}_{m\vec{K}}$ and $\psi^{PC}_{n\vec{k}}$ represent eigenstates of super- and primitive-cells, respectively. Similarly, $\vec{K}$ and $\vec{k}$ represent the wave vector of super-cell Brillouin zone and primitive cell Brillouin zone, respectively. $P_{m\vec{K}}(\vec{k})$ is the spectral weight, which gives the probability of eigenstates of super-cell that will be the same as the eigenstates of primitive cell. This bandUP technique is already used in graphene [50, 51] as well as nanowires [52].

Experimentally, the MXenes posses unique properties acquired from complex combined bonding nature and electronic structure, atomic stacking, synthesis condition, and surface termination [53]. Despite these fascinating properties and growing interest, the field lacks a systematic experimental investigation [17]. The poor structural stability of surface terminated nitride based MXenes are improved by making multi-layer structure, which has great applications in biology [54]. The excellent conductivity due to point defect predicted by DFT is conformed with the help of direct electrical measurements of single- and few-layer flakes of $Ti_3C_2T_2$ [27]. The robust $Ti_3C_2T_2$/S conductive paper/sheet with excellent conductivity, unique chemisorption, and mechanical properties of lithium polysulfide shuttle was fabricated through filtration-evaporation approach. $Ti_3C_2T_2$/S paper/sheet has excellent electrochemical properties [55]. The surface de-functionalization increased the electronic conductivity through in situ vacuum annealing, electrical biasing, and spectroscopic analysis within the transmission electron microscope [56].

Experimental and computational studies show that the nitride based MXene has great potential in the next generation electronic applications. However, there is a lack of systematic investigation in Ti_2N and its derivatives. Herein, we have focused on structural, electronic and magnetic properties of these MXenes.

RESULTS AND DISCUSSION

Structural Properties

The Ti_2N MXene is obtained by removing Al from hexagonal structure with space group number 194 ($P6_3$ / mmc) of Ti_2AlN MAX phase. The MAX phase is formed due to mixed combination of ionic/covalent/metallic bonding [57] between Ti, Al, and N atoms thereby hybridizing Ti $3d$-N $2p$, Ti $3d$-Al $3s$, and Ti $3d$-Al $3p$ states. The Al components in MAX phase are chemically reactive and the bonding between Ti and Al is purely metallic [58]. So, the relatively weak bond and reactive A element can be selectively etched with suitable chemical composition leaving behind the chemically stable closely packed Ti_2N MX phase. The chemical exfoliation of Ti_2N from Ti_2AlN usually leaves some -O, -F, -H, and -OH on the surface, and these groups may have significant influence on the electronic and magnetic properties of MXenes [11, 59, 60]. There are three possible sites of surface termination, on the top of Ti(1) (site a), on the top of N (site b), and on the top of Ti(2) (site c) (FIG. 5c). On the basis of these three sites, there are four possible configurations for the position of terminated species. In model I, at site a, in model II, at site b, in model III, at site c, and in model IV (mixed model II and III), one termination at site b and other termination at site c, are considered. The most preferential position for termination is in model III [61]. In the case of -OH termination, the favorable position of the hydrogen atom is on the top of oxygen atom, as a result, the structure becomes symmetrically equivalent to a mono-atom termination [37]. After the surface termination, there are electronic reconstruction of new energy states between Ti atoms with the terminated species.

To investigate the stability of bulk Ti_2AlN MAX phase, and bare Ti_2N and its corresponding functionalized Ti_2NT_2 (T= -OH, -H, -O, -F) MXenes, formation energy is calculated using formula,

$$E_f(Ti_2NT_2) = E_{tot}(Ti_2NT_2) - 2E_{bulk}(Ti) - E_{bulk}(N) - 2E_{bulk}(T)$$

where $E_{tot}(Ti_2NT_2)$, $E_{bulk}(Ti)$, $E_{bulk}(N)$, and $E_{bulk}(T)$

represent total energy of optimized systems, bulk energies of Ti, N, and T atoms, respectively [62]. In the similar way, cohesive energy is calculated as

$$E_c(Ti_2NT_2) = E_{tot}(Ti_2NT_2) - 2E_{iso}(Ti) - E_{iso}(N) - 2E_{iso}(T)$$

where $E_{tot}(Ti_2NT_2)$, $E_{atm}(Ti)$, $E_{atom}(N)$, and $E_{atom}(T)$ represent total energy of optimized systems, energies of isolated Ti, N, and T atoms, respectively. The energy of isolated atoms are calculated by adding single atom at the center of defined large super-cell [54]. The negative

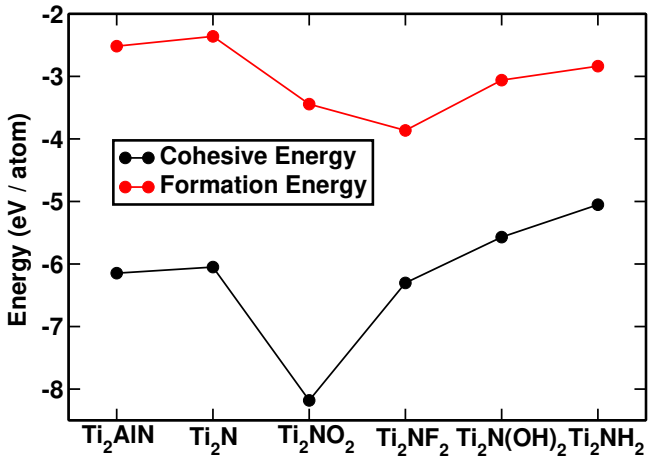

FIG. 2. (Color online) Formation and cohesive energies per atom of MAX phase, and bare and its corresponding functionalized MXene mono-layers. The negative values show the chemical stability of all MXenes and MAX phase. The oxygen and fluorine terminated MXene mono-layer is the most stable among all other MXenes and MAX phase.

value of the cohesive and formation energies indicate that our systems are stable and the oxygen and fluorine terminated MXenes are relatively more stable as compared to all other MXenes and MAX phase. This is mainly due to the strong hybridization between Ti-3d and O-2p. The formation energy is very large as compared to the cohesive energy of nitride based MXenes (Ti_2N and Ti_2NT_2), which is consistent with previously reported values [63]. So, it is difficult to extract nitride based MXene from its parent precursor MAX phase. From cohesive energy curve (FIG. 2), the stability increase in the sequence, Ti_2NH_2 < $Ti_2N(OH)_2$ < Ti_2N < Ti_2AlN < Ti_2NF_2 < Ti_2NO_2 [64]. But this sequence is quite different for the formation energy (FIG. 2): Ti_2N < Ti_2AlN < Ti_2NH_2 < $Ti_2N(OH)_2$ < Ti_2NO_2 < Ti_2NF_2. The bare MXene is less stable than the parent precursor MAX phase. We found that, the values of the formation and cohesive energies are significantly decreased after the surface terminations, particularly in -O and -F groups indicating the functionalized MXenes are more stable than the bare MXene. The Ti_2N MXene and its derivative structures have slightly lower formation energies than that shown in the Open Quantum Materials Database [65, 66]. Furthermore, the dynamical stability of Ti_2N was confirmed by phonon calculations. Here we find well separated optical and acoustic branches with no imaginary phonon frequency as in the Ref. [61] (FIG.3). With this finding and information, we use here the optimized mono-layered hexagonal structure [19].

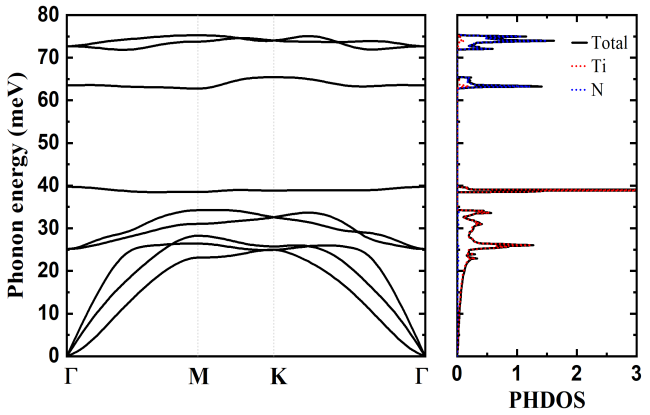

FIG. 3. (Color online) Calculated phonon dispersion along the high symmetry directions (Γ, M, K, and Γ) of the Brillouin zone (left) and the phonon PDOS (right) for Ti_2N mono-layer.

We first optimize our material systems, that makes easier to study the electronic and magnetic properties. Table I shows optimized lattice parameters, thickness of mono-layers (L), bond length between titanium atom Ti and terminated species T (d_{Ti-T}), titanium-titanium atoms (d_{Ti-Ti}), and titanium to nearest atom N (d_{Ti-N}) of selected functionalized MXenes. The calculated values are compared with previously reported theoretical values (shown in parenthesis) [19].

TABLE I. Calculated values of mono-layer thickness (L) and distance between Ti-T, Ti-Ti, and Ti-N atoms.

Crystals	L(Å)	d_{Ti-T}(Å)	d_{Ti-Ti}(Å)	d_{Ti-N}(Å)
Ti_2AlN	....	....	2.90	2.08
Ti_2N	2.31	....	2.87	2.06
Ti_2NF_2	4.57(4.63)	2.18(2.16)	2.77	2.08(2.07)
Ti_2NO_2	4.24(4.35)	2.00(1.98)	3.09	2.20(2.15)
Ti_2NH_2	4.23(4.20)	2.00, 2.01(2.00)	2.84	2.08(2.07)
$Ti_2N(OH)_2$	6.66(6.66)	2.17(2.17)	2.82	2.08(2.08)

Our optimized lattice parameters are in general consistent with the previously reported theoretical values (Figure 4) [19]. The extracted 2D MXenes from 3D MAX phase have decreased cell size, and bond length between Ti-Ti and Ti-N. But after the surface termination, the cell size and thickness of mono-layers are increased due to the addition of extra atoms in the bare Ti_2N MXene. The thickness of mono-layer strongly depends on terminating species. The thin mono-layer was found in hydrogen termination while thick mono-layer was found in hydroxyl

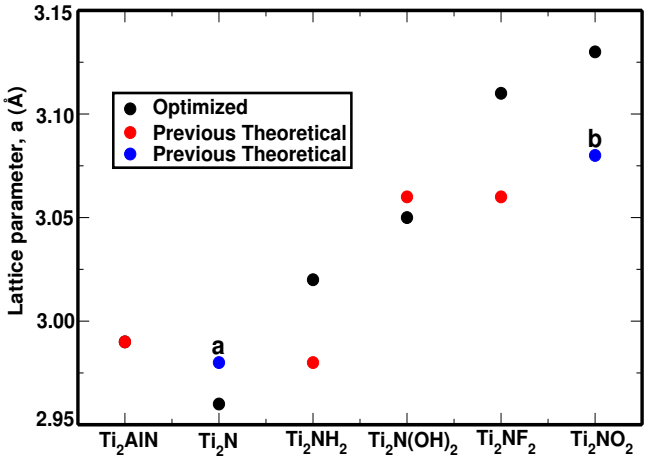

FIG. 4. (Color online) The optimized lattice parameters of MAX phase and MXenes. Red [19] and blue (a [64], b [54]) small circles represent previous theoretical values, and black small circles represent optimized lattice parameters of MAX phase, and bare and its corresponding functionalized MXenes. The optimized values of lattice parameters are in fair agreement with previously reported theoretical values.

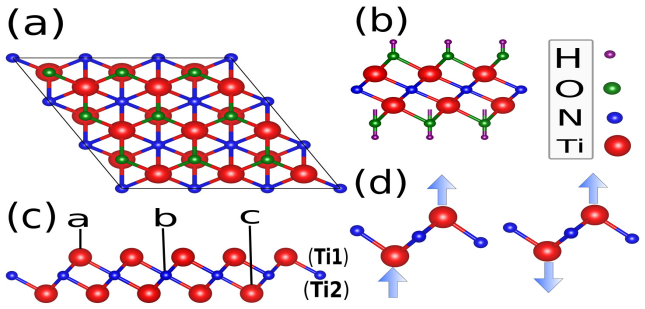

FIG. 5. (Color online) (a) The top view of Ti_2NO_2, and (b) and (c) are side views of $Ti_2N(OH)_2$ and Ti_2N in $3 \times 3 \times 1$ super-cells, respectively, (d) the side view of mono-layer Ti_2N. The up and down arrows indicate the up and down spins.

termination in the bare MXene. Interestingly, the bond length between Ti-N and Ti-T in Ti_2N, Ti_2NO_2, Ti_2NF_2, and $Ti_2N(OH)_2$ follow symmetrical bond nature except for Ti_2NH_2. In hydrogen termination, Ti-T bond length at the top side is slightly shorter than the bottom side. Meanwhile, the bond length between Ti and N atoms show symmetrical nature I.

The oxygen termination on MXene layers plays a remarkable role as compared to other terminated species. In oxygen termination, the bond length between Ti-Ti atoms increases by 0.22 Å and decreases by 0.1 Å in F termination but only slight change occurs in the case of -OH and -H terminations. Also, relatively shortest bond length d_{Ti-T} and longest bond length d_{Ti-N} represent strong interaction between surface of Ti and O atoms. The bond length between Ti-F is larger as compared to the other terminations, which shows weak interaction between Ti and F. The FIG. 5a and 5b represent the top and side views of the optimized structure of Ti_2NO_2 and $Ti_2N(OH)_2$ in $3 \times 3 \times 1$ super-cell. The terminated atoms are filling the vacant space on the top and bottom sides of Ti layers forming alternate position with titanium atoms in the stable configuration (FIG. 5b).

Electronic and Magnetic Properties Without Vacancy Defect

The energetically stable configurations of MAX phase, bare MXene and its corresponding functionalized MXenes have been studied with the full relaxed calculations corresponding to possible NM, FM, and AFM configurations. The MAX phase is energetically stable in NM configuration. In the case of bare MXene, the relaxation calculations with AFM configuration show zero net total magnetization with 0.33 μ_B magnetic moment for individual Ti atoms. Similarly, the relaxation calculations with FM configuration show total magnetization 1.10 μ_B per unit cell (with 0.25 μ_B magnetic moment for each Ti) which is closely comparable to 1.00 μ_B per unit cell found in Ref. [63]. The energy of FM and AFM configurations with reference to NM configuration are -39 meV and -36 meV, respectively. This shows, the FM configuration is energetically more stable than the AFM configuration.

It is interesting to point out that a few published papers (as for example Ref. [61]), especially in bare Ti_2N, indicate the AFM ground state by hypothetically using onsite electron-correlation (Hubbard U) on the top of PBE functional. They consider Hubbard parameter for titanium by burrowing the strong correlation effect of TiO_2 [67] in Ti_2N. Here, we focus on topology due to 2D nature and variable magnetism where the role of strong correlation may not be fully relevant. However, we tested Ti_2N with applying Hubbard parameter (4.2 eV as suggested by Ref. [61]) and found that the ground state becomes AFM with total loss of expected topological features in 2D materials. We used $1 \times 1 \times 1$, $2 \times 2 \times 1$, and $3 \times 3 \times 1$ cells to study the electronic band structure (with SOC) and the DOS without SOC. The surface termination on bare MXene mono-layer results the complete removal of magnetism except for the oxygen terminated one, which is 100% spin polarized half-metallic.

On moving from 3D bulk states (Ti_2AlN) to 2D surface states (Ti_2N), there are myriad changes in the electronic band structure and properties [63]. Interestingly, at the region between high symmetry points of K and Γ, there are two Dirac cones (a) (linear[68]) and (b) (distorted [68]) below the Fermi level in spin up channel, and two Dirac cones (c) (distorted) and (d) (linear) above the Fermi level in spin down channel (FIG. 6P). The formed gapless linear Dirac cones (a) and (d) may uncover the zero mass parameter but the distorted Dirac-like cones may reveal the non-zero mass parameter. It may be positive or negative, depending upon the nature of the distortion. The distorted Dirac cones (b and d) may suggest

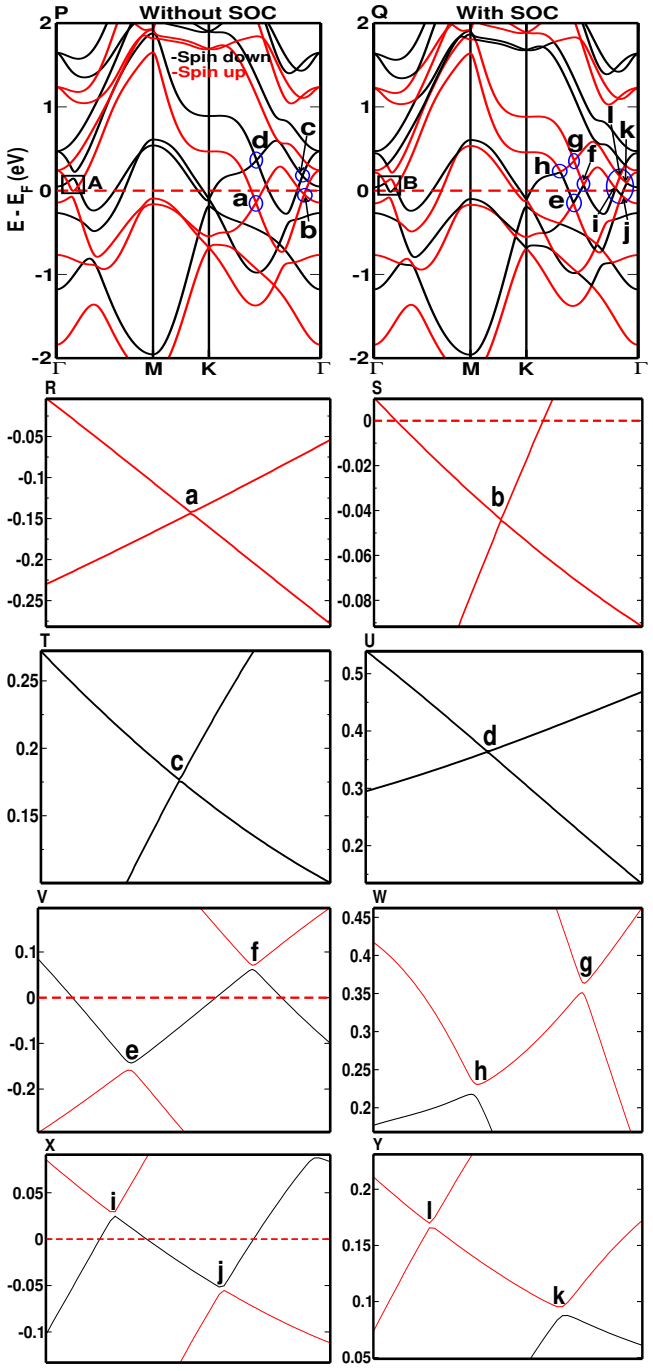

FIG. 6. (Color online) P and Q represent the spin polarized band structure corresponding to without SOC and with SOC of bare Ti_2N MXene mono-layer, respectively. R, S, T, U, V, W , X, and Y highlight the band crossings including Dirac-like cones. A and B indicate the band inversions, which are highlighted in FIG. 7. The red dashed lines represent the position of the Fermi level.

positive mass parameter [68]. The formation of distorted Dirac-like cone apparently diminishes the characteristic of the quantum oscillation as prescribed in Ref. [35]. The formation of Dirac cone (b) just below the Fermi level reveals the idea of n-type self doping character informing the presence of electron carriers even without transforming the electrons from surrounding environment [31]. The spin down bands show the metallic character whereas the spin up bands show weakly half-metallicity indicating that Ti_2N is weakly half-metallic as suggested by Ref. [63]. The same band crosses the Fermi level multiple-times forming multiple Dirac cones at and near the Fermi level suggesting multi-nodal properties in Ti_2N [69]. The bottom of unoccupied states in the spin down and top of occupied states in the spin up channels lie just above and below the Fermi level, which reveal the exchange splitting energy of 0.16 eV (FIG. 6P) [70]. This exchange splitting is caused by the $3d$ states of Ti atom. The band structure corresponding to SOC in Ti_2N is shown in FIG. 6Q. The overlapped bands (without SOC) near the Fermi level in region Γ-M are separated and form Dirac topological features under the presence of SOC without disturbing the multi-nodal properties. Interestingly, the SOC allows to make two gapped linear Dirac cones (e) and (f) below and above the Fermi level (FIG. 6Q). The formation of Dirac cone just above the Fermi level reveals the self p-type doping character [31, 35]. The origin of gap opening in the Dirac cones are due to hybridization of the electronic wave function between the top and bottom surfaces with the same quantum numbers[71]. In our case, the hybridization causes the time reversal symmetry breaking under SOC [72] and the Dirac cones behave massive states [73, 74]. Similarly, linear gapped Dirac cone (i) and distorted gapped Dirac cone (j) are found near the Fermi level (above and below) in region K-Γ (FIG. 6Q). In the same region, a linear gapped Dirac cone (l) and distorted gapped Dirac cones (g), (h), and (k) are found above the Fermi level.

Figure 7 shows the zoomed view (A and B) of FIG. 6 with spin polarized projected $3d$ band structure of Ti atom in Ti_2N MXene. It has octahedral symmetry (D_{3d}), where the t_{2g} (d_{xz}, d_{yz}, and d_{xy}) and e_g ($d_{x^2-y^2}$ and d_{z^2}) are lower and higher energy states, respectively [26, 75]. The d_{xy} of t_{2g} and d_{z^2} of e_g states juxtapose each other and in the absence of SOC, the spin up and down bands cross at two points (I and II).

The SOC couples the opposite spin components forming the topologically non-trivial gap at the band crossing points (I and II) [76–79] (FIG. 7B). The gap opening results from the time reversal symmetry breaking [72] and hybridization [71] of the opposite spin states (FIG. 7B). Here, the d_{xy} state is hybridized with the d_{z^2} state around I and II. Thus, the hybridization also plays a vital role to open the gap under the application of SOC. The gap opening in I is relatively larger as compared to II. The dispersion of the bands remain linear under the SOC. The non-trivial topological gap with $Z_2 = 1$ [80, 81] (as in Bi/Sb(111) [82] and RuClBr [83]) form the linear Dirac cones, which are responsible for the quantum oscillations [35]. Thus, Ti_2N is expected as a topological

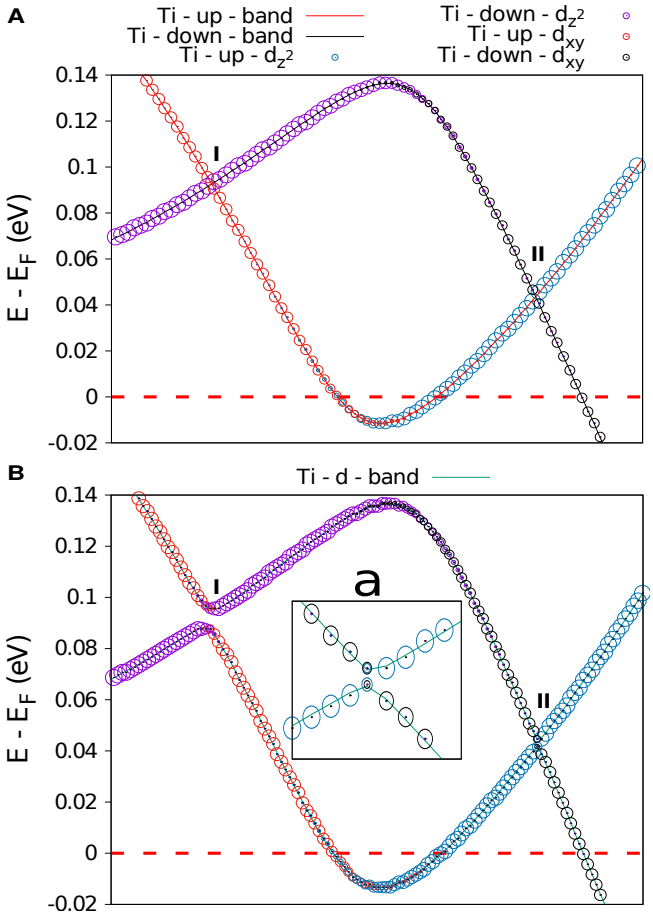

FIG. 7. (Color online) A (without SOC) and B (with SOC) represent the projected spin polarized $3d$ band structure of Ti atom of Ti_2N in $1 \times 1 \times 1$ mono-layer. The spin up and spin down bands are mixed states of t_{2g} (d_{xy}) and e_g (d_{z^2}), respectively. In the absence of SOC, the bands are crossing at two different points. The SOC opens a topologically non-trivial gap at the band crossing points (I and II) forming band inversions. These band inversions are due to hybridization of d_{xy} from t_{2g} and d_{z^2} from e_g at I and II points, respectively. The colored points indicate the spectral weight of each states in the band structure. Inset (a) represents the zoomed view of the gap opening at point II. The dashed red line represents the position of the Fermi level.

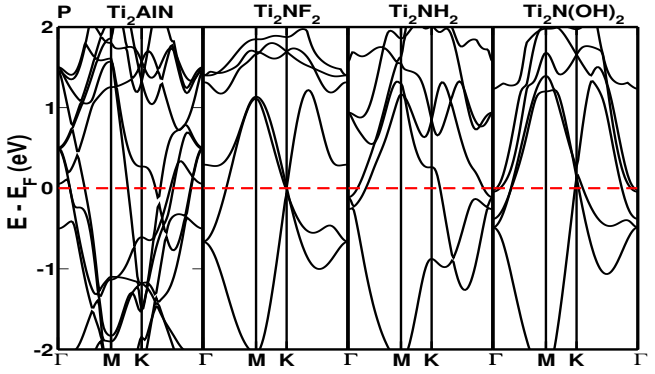

FIG. 8. (Color online) P represents the band structure of Ti_2AlN MAX phase and functionalized Ti_2NT_2 (T = -F, -H, -OH) MXene mono-layers. The red dashed lines represent the position of the Fermi level.

material [84]. In the same vein, just above the Fermi level in the region K - Γ, the band inversions are uncovered indicating non-trivial topological features (f and i representations in FIG. 6Q), whose characteristic features are already discussed above. These unprecedented multiple or double band inversions around the Fermi level are resulted from the nodal lines [85].

The overlap of the valence and the conduction bands at the Fermi level in band structure (FiG. 8) of MAX phase reveals the considerable metallic character. The presence of SOC does not influence these outcomes. After surface termination, all the functionalized Ti_2NT_2 (T = -OH, -H, -F) MXenes become metallic NM [19] except for oxygen terminated one, which is half-metallic ferromagnet (FiG. 9) [10]. The electronic properties of Ti_2NF_2 and $Ti_2N(OH)_2$ are similar due to the presence of electrophiles -F and -OH, which accept one electron from Ti. However, the electronic property of Ti_2NO_2 is different due to the presence of -O electrophile, which accepts two electrons from Ti atom [60].

The band structure of hydrogen terminated MXene in $1 \times 1 \times 1$ mono-layer is shown in FIG. 8. The band splitting from a Γ point is reconstructed at another Γ point just below the Fermi level. Further, the bands cross the Fermi level from the occupied states to the unoccupied states, thereby converting the weakly half-metallic Ti_2N to metallic.

The bands cross the Fermi level from the occupied states to the unoccupied states indicating the metallic property in both -F and -OH terminated mono-layer (FIG. 8) similar to that of H terminated one. Astonishingly, gapped Dirac cones are found at K point on and above the Fermi level in the case of -F and -OH terminations, respectively (FIG. 8). The charge carrier corresponding to that Dirac cone behaves like hole-pockets at the conduction band [35].

Similarly, the oxygen termination converts the weakly half-metallic to 100% spin polarized half-metallic (FIG. 9). The spin up and the down bands are with similar characters (FIG. 9P). The spin down channel clearly shows the semi-conducting nature whereas the spin up channel shows the metallic nature exhibiting the half-metallic character. The half-metalicity is conformed by calculating the band structure using HSE06 (FIG.10A). The HSE06 increased the difference between the Fermi level and the bottom of unoccupied spin down band from 0.03 eV to 0.51 eV as compared to that of PBE (FIG. 10B). This half-metallic FM nature is due to the exchange splitting energy of 0.42 eV, which is higher than that found in the Ti_2N mono-layer. The spin down band splits from the near Γ point above the Fermi level and recon-

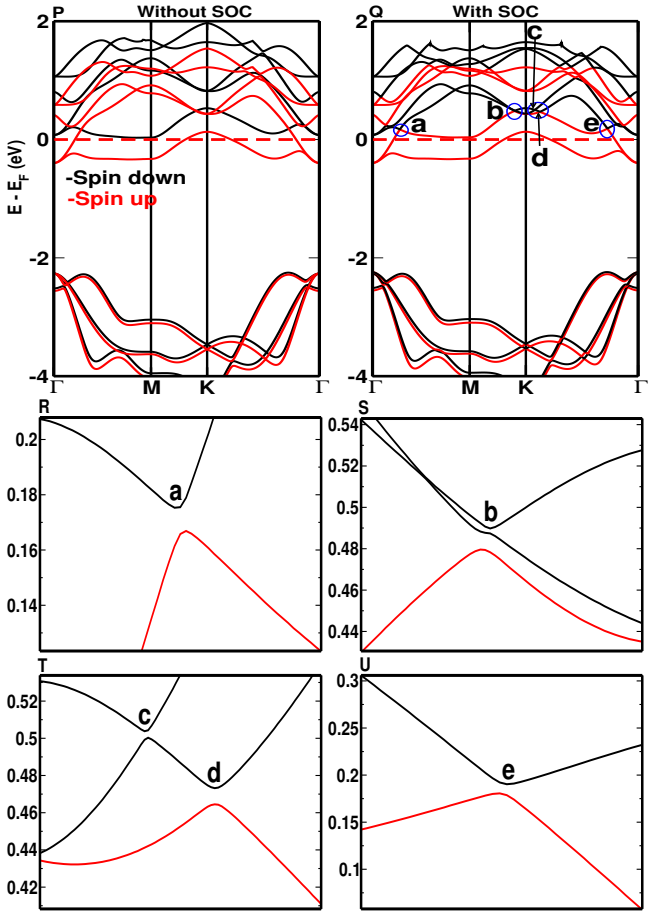

FIG. 9. (Color online) P and Q represent the spin polarized band structure corresponding to without SOC and with SOC of oxygen terminated Ti_2NO_2 MXene mono-layer. R, S, T, and U highlight the Dirac features. The red dashed lines represent the the position of the Fermi level.

structs at another Γ point above the Fermi level. Same behavior happens for the spin up band starting from below the Fermi level. The presence of SOC in Ti_2NO_2 mono-layer converts the half-metallic to topological half-metallic nature (FIG. 9P). Interestingly, four distorted gapped Dirac cones such as: three (b, c, and d) and one (a) are found at the vicinity of K and Γ above the Fermi level, respectively. Similarly, a linear gapped Dirac cone (e) is found at the region between K - Γ just above the Fermi level.

On moving from primitive to super-cells, the multiplex topological features of folded band structures [86] have been calculated. These complex folded band structures of super-cells are unfolded to conform the band structures emerging from the primitive cell (FIG. 11). The folded bands are difficult to analyze with the angle-resolved photoemission spectroscopy data [48, 86]. Thus, the unfolding of the band structures are important to analyze and compare with the experiment.

To get better deliberation on the electronic properties

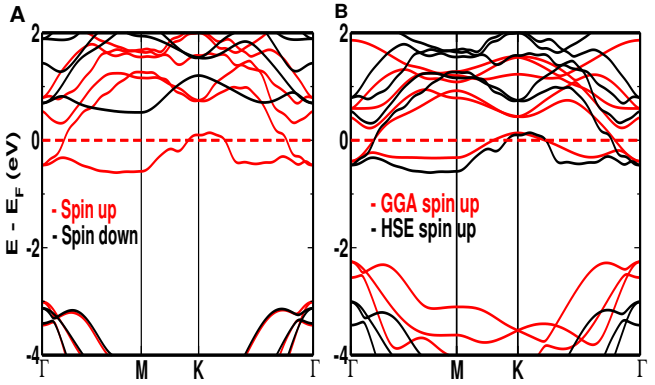

FIG. 10. (Color online) Figure (left) shows the spin polarized band structure of Ti_2NO_2 using HSE06 and figure (right) shows the comparison of spin down bands between HSE06 and GGA methods. The spin down band (in GGA) is calculated by using wannier function. The red dashed lines represent the the position of the Fermi level.

of MAX phase and MXenes, PDOS are shown in FIG. 12. The bands of MAX phase are mainly contributed from Ti-3d, N-2p, Al-3p, and Al-3s states. The total DOS is dominated by Ti-3d states. The 3s and 3p states of Al, and 2p and 2s states of N form a very large energy gap of 6.49 eV, which is consistent with previously reported value of 6.2 eV [87]. This large energy gap in valence band indicates that there is no sp hybridization in Ti_2AlN. The value of DOS near the Fermi level N(E_F) is 2.74 states per eV, which is also consistent with the previously reported value of 3.03 states per eV [88].

To illustrate the electronic properties vividly, we divided the valence band into two sub-bands of A and B (FIG. 12P). In the sub-band A, there is a strong contribution from Ti-3d and Al-3p states. Similarly, in the sub-band B, the strong contribution is from the Ti-3d and N-2p states and weak contribution is from the Al-3s states. So, the Ti-3d states play a significant role in both sub-bands A and B.

After eliminating Al from MAX phase, bands become narrow and form large indirect gap of 2.40 eV in the spin up and 2.59 eV in the spin down (within the occupied part) between the sub-bands A and B in Ti_2N. The sub-band A is formed due to strong contribution from Ti-3d states and weak contribution from N-2p states. Similarly, the sub-band B is formed due to the combination of N-2p states and Ti-3d states with major contribution from N-2p states. This may indicate that, the change occurring below the Fermi level influences the electronic states at the Fermi level as discussed earlier in Ref. [89].

The termination on mono-layer MXene plays a vital role especially far below the Fermi level in the valence band. The surface termination in the bare MXene mono-layer splits the sub-band B into separate sub-bands B and C. In fluorinated mono-layer, the sub-band A is dominated by Ti-3d states and the sub-bands B and C are the

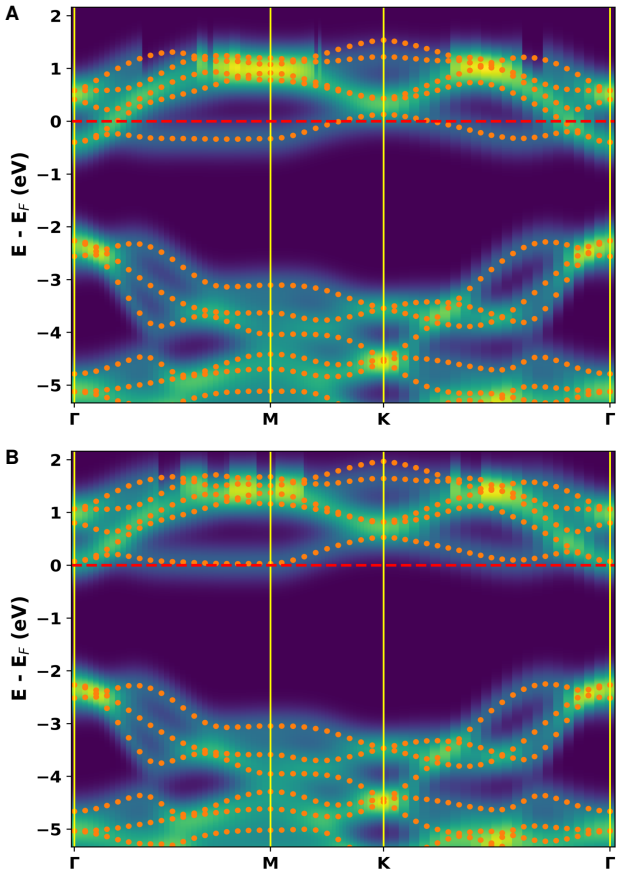

FIG. 11. (Color online) A and B represent the spin up and spin down band structure of unfolded 3 × 3 × 1 super-cell and primitive cell to revive the effective primitive band structure of Ti_2NO_2. The colored (orange) dotted curves represent the effective bands of primitive cell and shaded spectral bands (green and yellow) represent the total spectral weight of unfolded bands of the super-cell. The sharp yellow colored bands reveal the higher spectral weight. The red dashed lines represent the position of the Fermi level.

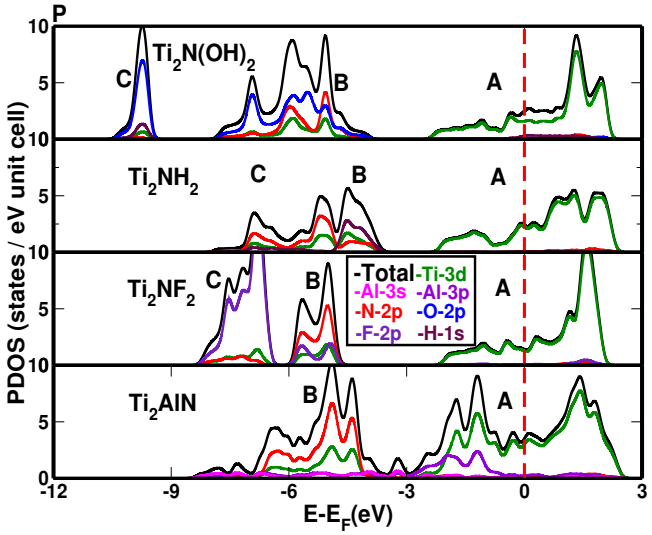

FIG. 12. (Color online) P represents the PDOS of Ti_2AlN MAX phase and Ti_2NT_2 (T = -F, -H, -OH) MXene monolayers (with gaussian smearing). The red dashed line represents the position of the Fermi level.

mixed of Ti-3d, N-2p, and F-2p states (FIG. 12P). The sub-band C is significantly dominanated by F-2p states. The large indirect energy gap of 2.71 eV and comparatively small direct energy gap of 0.74 eV appear in between the sub-bands A and B, and the sub-bands B and C, respectively.

Hydroxyl termination follows the similar trend in which the sub-band A is dominated by Ti-3d states. The sub-band B is the mixed states of Ti-3d, N-2p, and O-2p states but the sub-band C is the mixed states of O-2p, Ti-3d, and H-1s, and N-2p states (FIG. 12P). The indirect energy gap of 1.65 eV and the direct energy gap of 1.84 eV are found between the sub-bands A and B, and B and C, respectively.

Similarly, the sub-band A in H and O terminated MXenes are also dominated by Ti-3d states (FIG. 12P). The hydrogen atom contributes only in the sub-band B (FIG. 12P). In hydrogen termination, only one indirect energy gap of 1.53 eV is found between sub-bands A and B, and continuous bands are found between the sub-bands B and C. Likewise, in oxygen termination, the small direct energy gap of 0.13 eV in the spin up and 0.09 eV in the spin down are found between the sub-bands B and C exhibiting the strong hybridization between Ti-3d, N-2p, and O-2p states. But the large indirect energy gap of 1.88 eV in the spin up and 2.22 eV in the spin down are found between the sub-bands A and B. The sub-band C is mainly dominated by O-2p states (FIG.14).

From the electronic band structure, the Fermi level is shifted down in the bare MXene obtained by etching Al from the MAX phase and is again shifted down under the surface terminations. The sub-band C is found below the sub-band B, due to electronic reconstruction between Ti and functional group. The functional group mainly contributes in both sub-bands B and C except for hydrogen termination, where hydrogen atom significantly contributes only in the sub-band B (FIG.12P).

Origin of Half-metallic Gap in Ti_2NO_2

The magnetism and half-metallicity strongly depends upon the coordination environment of Ti and the number of 3d electrons associated within it. It plays a vital role in the electronic and magnetic properties. Similar to TM dichalcogenides, non-bonding 3d bands in MXenes are positioned between the bonding and anti-bonding of Ti-N and Ti-O states [90]. Presuming all the constituent elements (N and O) are in their normal oxidation states O^{2-} and N^{3-}, the Ti-N and Ti-O bonding states are completely filled, while their anti-bonding states are empty. So, only the presence of 3d electrons in the non-bonding

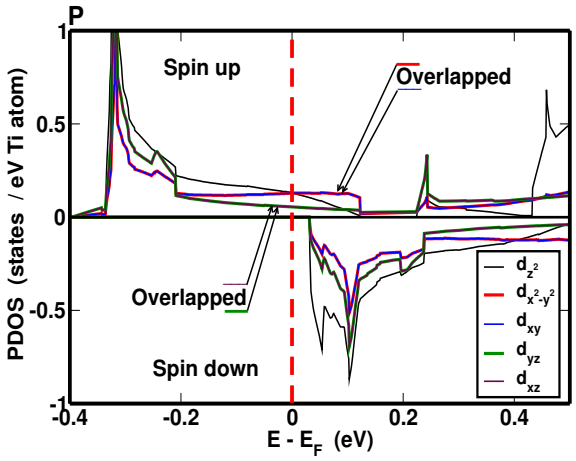

FIG. 13. (Color online) P represents the projected spin polarized $3d$ DOS of Ti in Ti_2NO_2 within $1 \times 1 \times 1$ mono-layer using tetrahedron integration method. The Ti atom follows the octahedral symmetry (D_{3d}) crystal field from neighboring N and O, which split the $3d$ orbital into t_{2g} (d_{xz}, d_{yz}, and d_{xy}) and e_g ($d_{x^2-y^2}$ and d_{z^2}) states. The red dashed lines represent the position of the Fermi level.

states are able to contribute to the magnetism of Ti_2NO_2. In Ti_2NO_2, the Ti atom subjected to octahedral crystal field (with symmetry D_{3d}) from neighboring N and O atoms. As shown in FIG. 13, E_g corresponds to (x^2-y^2, xy) and (xz, yz) degenerate states, whereas $A_{1g}(z^2)$ form a separate state Refs. [90, 91]. The magnetism appearing in this class of materials are due to mixed localized and delocalized characters of Ti-$3d$ instead of electron counting applied in Refs. [10, 90].

Figure 13P details the projected spin polarized $3d$ DOS of Ti in Ti_2NO_2 using tetrahedron integration method. The d_{xy} and $d_{x^2-y^2}$ states form a degenerate state whereas d_{xz} and d_{yz} states also form another degenerate state. The three multiplets are formed by d_{z^2}, d_{xy} and $d_{x^2-y^2}$, and d_{yz} and d_{xz}. Individually, the non-degenerate d_{z^2} state dominates the other states in both spin channels. The d_{z^2} state crosses the degenerated states $d_{x^2-y^2}$ and d_{xy} exactly at the Fermi level. The concept of t_{2g} and e_g states breaks down due to the local symmetry, which is responsible for the half-metallic character in Ti_2NO_2.

The top and bottom layers of Ti provide two electrons to O atoms in respective sides and they jointly (both bottom and top of Ti layers) provide three electrons to the neighboring N atoms. Due to lattice symmetry, there is equal possibility for +4 and +3 oxidation states of Ti in the top and bottom layers. The remaining one $3d$ electron either fills the non-bonding states or helps to delocalize the system to have band magnetic feature and telltale the magnetic moment of 0.27 μ_B per Ti atom. This magnetic moment splits the above mentioned states into fully occupied bands for majority spin channel and open bands for minority spin states providing the semiconducting nature with large gap of 2.28 eV in the minority spin channel, which is also availed by Ref. [10]. The material with large half-metallic gap is most promising magnetic material for the next generation 2D spintronics [92, 93].

Effect of Biaxial Strain in Electronic Band Structure of MXene

Here, we have studied the compressive strain a(1-e) and the tensile strain a(1+e) (where, e represents compression and elongation up to 5% with increment of 1%) keeping the fixed value of the vertical distance (vacuum) of 17.04 Å. Under the compression in $Ti_2N(OH)_2$ (up to 5%), the Fermi level is shifted up continuously by pushing the electrons from the occupied states to the unoccupied states. The distorted Dirac cone is found at K point above the Fermi level, which remains distorted under 1% compression. Additionally, on increasing the compressive strain from 1%, the distorted gapped Dirac cones change to linear type (in 2%, 3%, and 4%) and finally returns to the original features under 5% compression. Again, the complex band crossings are also found in the region between K-Γ below the Fermi level under compression from 2% to 5%.

Unlike the compression, the scenario of shifting the Fermi level is reversed during the tensile strain. The Fermi level is continuously shifted down under tensile strain indicating the electrons are pushing from the unoccupied states to the occupied states. While increasing the strength of tensile strain, the gapped Dirac cone gets enhanced. We have also studied the effect of applied compression and tensile strains in the bare Ti_2N MXene and other surface terminated MXenes. Ti_2N , Ti_2NF_2, and $Ti_2N(OH)_2$ show the same physics for shifting the Fermi level whereas Ti_2NH_2 shows the opposite trend. Under the compression, two Dirac cones have been found below the Fermi level in the region K-Γ whereas only one Dirac cone has been found under the tensile strain in Ti_2NH_2.

The half-metallic nature in oxygen termination shows peculiar electronic and magnetic properties. The half-metallicity is extremely sensitive to compression. It breaks down under 1% compressive strain.

Under the compression, the spin down channel is shifted from the unoccupied states to the occupied states whereas the spin up channel is shifted toward the unoccupied states from the occupied states and finally both bands are overlapped under 5% compression by converting the system from FM to NM states (FIG. 14). This situation is completely reversed under tensile strain, while increasing the tensile strain, the spin down channel is continuously shifted towards the unoccupied states whereas the spin up channel is continuously shifted towards the occupied states preserving half-metallic character (FIG. 14). In the spin up channel, the bands degenerated from Γ point cross the Fermi level in strain free states and reconstruct at other Γ point. The degen-

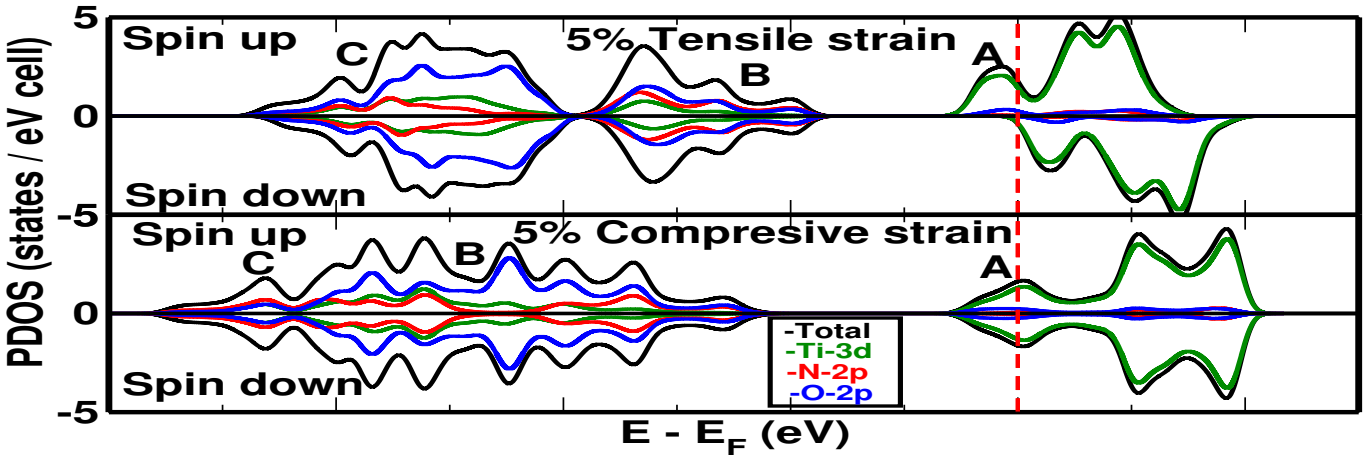

FIG. 14. (
Color online) PDOS (left) and band structure (right) under 5% compressive and tensile strains in Ti_2NO_2 MXene. A, B, and C in PDOS represent the sub-bands below the Fermi level.

erated lower band in up channel just touches the Fermi level at K point under 3% tensile strain. Further, increasing the tensile strain, it completely shifts towards the occupied states. The robustness and mutable nature of half-metallic ferromagnetism under applied strain is also clearly shown in FIG. 14.

Vacancy Defect in Ti_2NO_2 MXene

Before studying the electronic and magnetic properties of defected systems, the structural stability corresponding to different super-cells has been studied. The formation and cohesive energies of mono-layer Ti_2N reveal the structural stability starting from $2 \times 2 \times 1$ super-cell. So, the structural defects can be studied within the framework of $2 \times 2 \times 1$ super-cell. Herein, we have studied the single vacancy defect and doping in relatively most stable configuration of Ti_2NO_2.

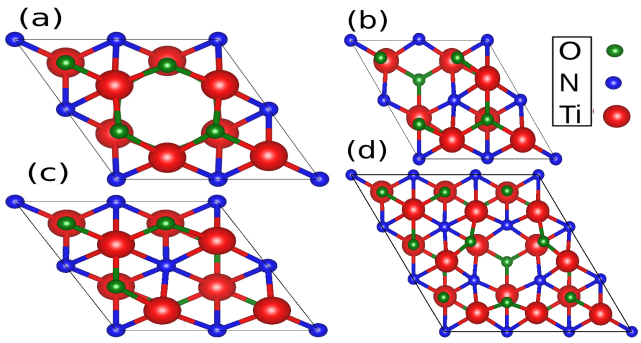

FIG. 15. (Color online) (a), (b), and (c) are top view of single N, Ti, and O vacancy defects within Ti_2NO_2 MXene in $2 \times 2 \times 1$, respectively and (d) is single vacancy defect of Ti in $3 \times 3 \times 1$ super-cell.

The vacancy concentration defects with N (25%), O (12.5%), and Ti (12.5% and 5.5%) have been investigated. The magnetic and NM calculations show NM as the ground state for all defected systems. Therefore, NM configuration was considered to investigate the properties of defected systems using $2 \times 2 \times 1$ and $3 \times 3 \times 1$ super-cells. The relaxed structures corresponding to N, O, and Ti in Ti_2NO_2 are shown in FIG. 15. In defect free Ti_2NO_2, the bond length between Ti and N follows symmetrical nature in the entire super-cell. Under the defect formation, the global symmetry is destroyed preserving the local symmetry structures. The formation energy of single vacancy defect is calculated by using formula,

$$E_{SV} = E_{pure} - (E_{defect} + \frac{E_{bulk}}{M})$$

where E_{pure} and E_{defect} are the total energy of defect free and defected systems, respectively. Similarly, E_{bulk} is the bulk energy of atom forming defect in system and M is total number of atoms in bulk [26]. The formation energies of single vacancy defects follow the sequence V_{Ti}-Ti_2NO_2 > V_O-Ti_2NO_2 > V_N-Ti_2NO_2. The Ti defect formation is more energy consuming as compared to others because it requires six bonds to break (three Ti-N and three Ti-O). In Ti($3d$)-O($2p$) overlap, the Ti is in +4 oxidation state. This oxidation state in Ti_2NO_2 leads to strong Ti-O bond [26]. Due to this reason, Ti-O bond is relatively stronger than Ti-N bond. Similarly, O defect requires the breaking of only three Ti-O bonds resulting in relatively less energy consumption than that of Ti defect. The N defect requires breaking of six Ti-N bonds. These Ti-N bonds are relatively weaker as compared to Ti-O bonds, so N defect is relatively less energy consuming as compared to Ti and O defect in Ti_2NO_2 MXene sheet. We have also used larger $3 \times 3 \times 1$ super-cell to get more insight in the Ti defected system. While moving from $2 \times 2 \times 1$ to $3 \times 3 \times 1$ super-cell, the formation energy increases by 0.96 eV designating $2 \times 2 \times 1$ super-

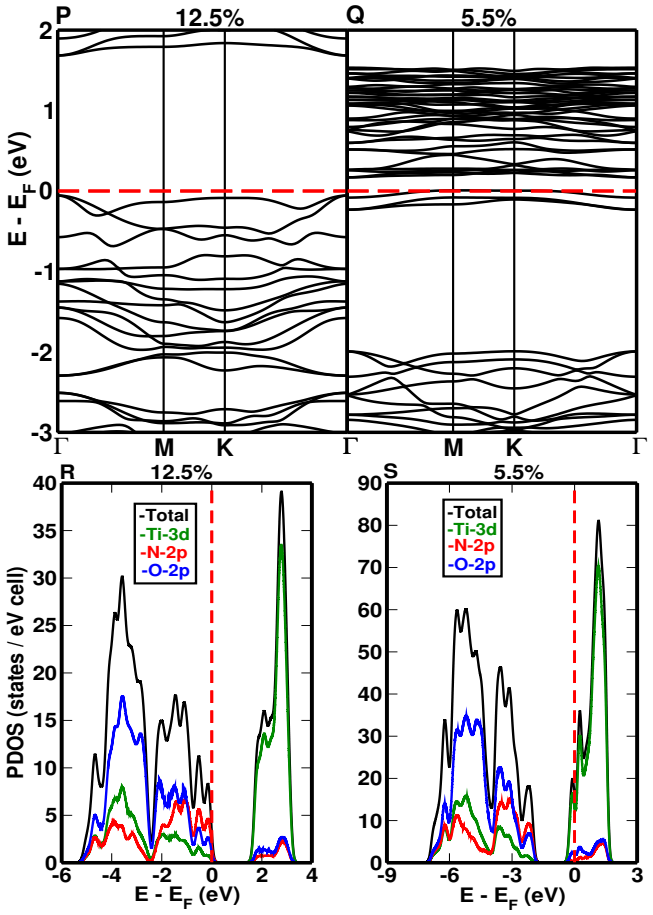

FIG. 16. (Color online) P and Q are the band structure, and R and S are PDOS of single vacancy of Ti in 2 × 2 × 1 and 3 × 3 × 1 super-cells of Ti_2NO_2 with vacancy concentration 12.5% and 5.5%, respectively. The red dashed lines represent the position of the Fermi level.

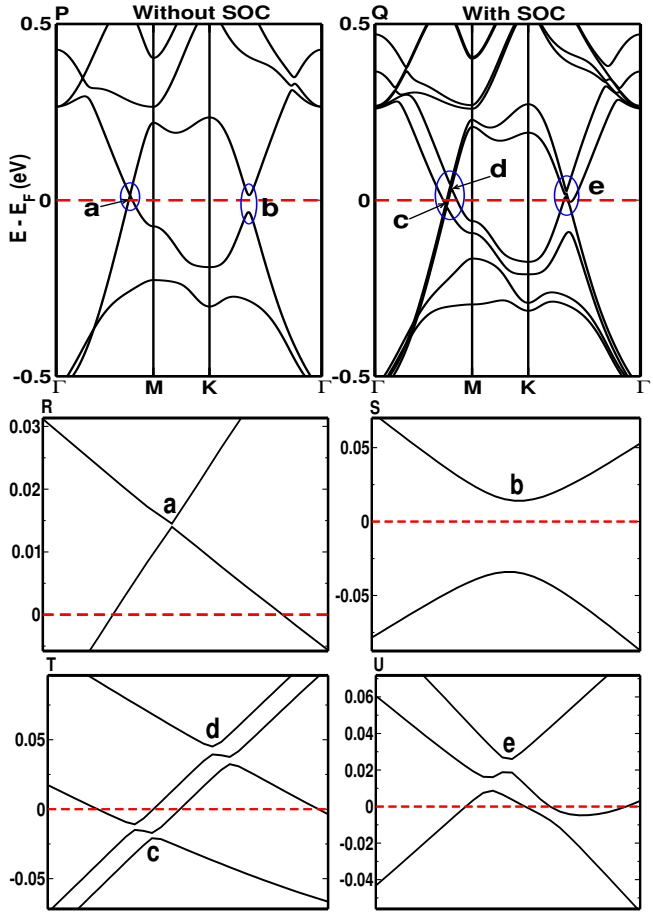

FIG. 17. (Color online) P and Q represent the band structures corresponding to without SOC and with SOC with 12.5% vacancy concentration of O within 2 × 2 × 1 super-cell in Ti_2NO_2, respectively. R, S, T, and U highlight the Dirac cones. A slightly distorted Dirac cone (a) is found just above the Fermi level, which telltale the p-type self-doing character diminishing the quantum oscillation. Interestingly, a gapped Dirac cone (b) is found at the Fermi level, which may exhibit paramount transport properties in the system. The red dashed lines represent the position of the Fermi level.

cell more stable than 3 × 3 × 1 super-cell in Ti defected system.

With the appropriate ground state energy, the electronic band structure and DOS were studied. Interestingly, the single vacancy defect of Ti and O atoms in Ti_2NO_2 abruptly changes the electronic properties from the half-metallic to the semi-conducting with large direct band gap of 1.73 eV in 12.5% for Ti and semi-metal in O defect, which are consistent with previously reported theoretical results [26]. The semi-conducting nature found in Ti defect changes to weak semi-conductor under vacancy concentration of 5.5%. So, the concentration of vacancy defect eloquently changes the electronic properties of MXene. On decreasing the concentration of vacancy defect, the Fermi level is shifted towards conduction side exhibiting perfect semi-conductor to weak semi-conductor for Ti defect (FIG. 16Q). The NM solution of band structure for O defect with vacancy concentration of 12.5% is shown in FIG. 17. The semi-metal is found by forming two Dirac cones (a) just above the Fermi level and (b) at the Fermi level. The formation of Dirac cone at the Fermi level enhances the transport properties of electrons in the system [33]. The Dirac cone above the Fermi level reveals the characteristic of the p-type self-doping [31]. Here, due to the SOC, the bands split and form multiple Dirac features (c) and (d) below and above the Fermi level revealing the n- and p-type self doping characters, respectively. Similarly, the split bands form multiple distorted Dirac features (e) near the Fermi level, which also enhance the transport properties. The formation of the distorted Dirac cone diminishes the quantum oscillation [35]. The N defect changes the half-metallic nature to the metallic, which is also consistent with previously reported theoretical results [26]. The gapped linear Dirac cone (a) is found in the region of Γ-M above the Fermi level (FIG. 18P). Similarly, a linear gapless Dirac

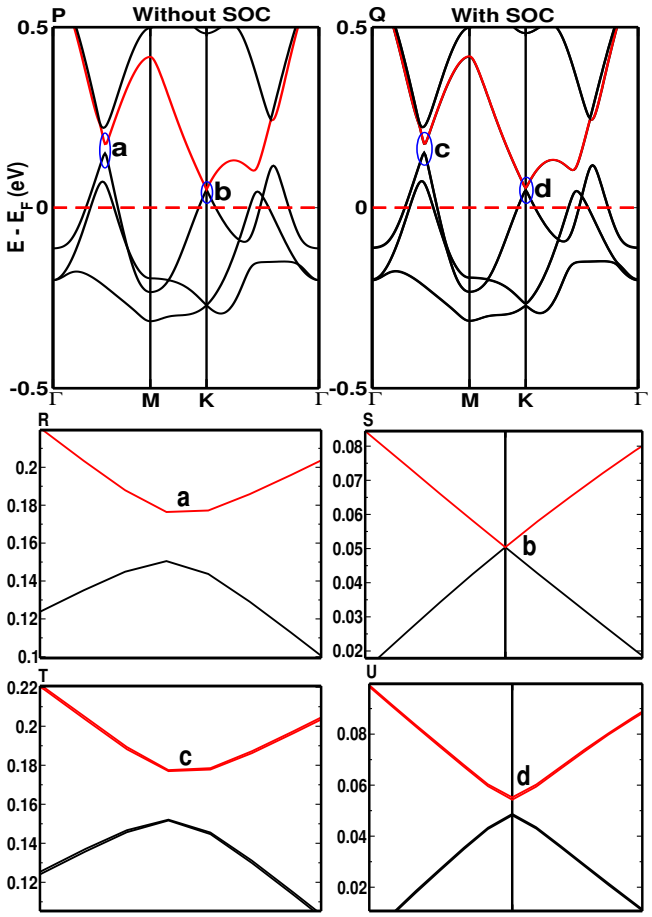

FIG. 18. (Color online) P and Q represent the band structures corresponding to without SOC and with SOC with 25% N vacancy concentration in Ti_2NO_2, respectively. R, S, T, and U highlight the Dirac features. The red dashed lines represent the position of the Fermi level.

cone (b) is found at K point above the Fermi level. Applying the strength of SOC on Ti atoms, the bands get split and opened at about 0.01 eV in the Dirac cone (b) (FIG. 18U) [91]. Thus, the SOC converts the massless Dirac feature (b) to massive gapped Dirac feature (d) by forming the gap between the top and bottom surface states[73]. Furthermore, we have also studied the O and N vacancy defects in $3 \times 3 \times 1$ super-cell. In both cases, the metallic nature is revealed.

To get better delineation on the electronic band structure of Ti defect in $2 \times 2 \times 1$ and $3 \times 3 \times 1$ super-cells, the PDOS are shown in FIG. 16(R and S), respectively. In both super-cells, the conduction band near the Fermi level are mainly dominated by Ti-3d states. Similarly, the valence bands consist of Ti-3d, O-2p, and N-2p states with dominant character of O-2p states. The PDOS of O defect is shown in FIG. 19P. The bottom of valence bands are mainly dominated by N-2p and O-2p states, whereas the conduction bands are significantly dominated by Ti-3d states and trivial contribution from N-2p and O-2p

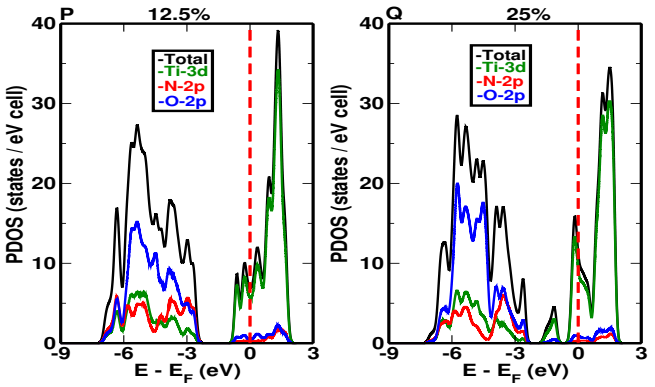

FIG. 19. (Color online) P and Q represent the PDOS of O and N defects with vacancy concentrations of 12.5% and 25% in Ti_2NO_2. The red dashed lines indicate the position of the Fermi level.

states. Under the O defect, the Fermi level is shifted toward the unoccupied states forming the semi-metal. Figure 19Q shows the PDOS of N defect in Ti_2NO_2. Similar to the O defect, the valence bands are dominated by O-2p and N-2p states, whereas the Ti-3d states dominate around and above the Fermi level.

Influence of Cr, Mn, and Co Doping in Ti_2NO_2 MXene

Here, we performed the substitutional doping (12.5%) of different transition elements such as Cr, Mn, and Co in Ti_2NO_2 MXene within $2 \times 2 \times 1$ super-cell. The substitution of TM elements break the bond length symmetry.

Under the Cr substitution, the global symmetry in bond length breaks down with slight changes. However, local symmetry is preserved near the dopant atom. The Cr-N bond length is 2.09 Å, which is slightly shorter than that of Ti-N in pristine phase, whereas the Cr-O bond is 2.09 Å, which is slightly larger than that of Ti-O in pristine. The elongation and compression of Cr-O and Cr-N bonds, as compared to pristine, significantly break the uniformity in the bond length throughout the super-cell.

In the case of Mn dopant, same behaviors are found with slight variation in the bond length. But for Co, the bond length between Co-O is 2.27 Å, which is larger by 0.27 Å as compared to Ti-O in pristine phase. Similarly, the Co-N bond is 2.08 Å, which is shorter by 0.12 Å than that of Ti-N. The elongation and compression in the bond length result the Co atom slightly shifted towards the bottom side (FIG. 20c). The relaxed structures after substitutions of Mn, Cr, and Co in Ti_2NO_2 are shown in FIG. 19. The stability of doped systems were investigated through the formation energy using the formula,

$$E_f = (E_{t1} - E_{t2}) - (E_1 - E_2)$$

where E_{t1} and E_{t2} represent the total energies of Ti_2NO_2 with substitutional and pristine phases. E_1 and E_2 represent the free energy of single dopant and Ti atoms [94].

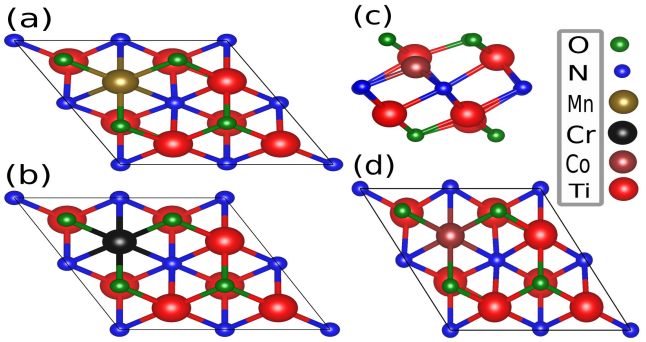

FIG. 20. (Color online) (a) and (b) are top views of Mn, Cr doped, and (c) and (d) are side and top view of Co doped in Ti_2NO_2.

The calculated value of formation energies are 4.43 eV, 3.70 eV, and 3.81 eV in Mn, Cr, and Co doped MXenes, respectively [95]. The positive values of the formation energies of Mn, Cr, and Co doping in Ti_2NO_2 indicates that the pristine composition is relatively easier to form than the doped ones as indicated in Ref. [95]. The substitution of transition metals in MXene sheets inaugurate the significant change in the structural, electronic, and magnetic properties while favoring the specific magnetic configurations.

Figure 21 (P and Q) represents the spin polarized band structure and PDOS of Mn doped system. The Mn in Ti_2NO_2 allows to convert 100% spin polarized half-metallic to weakly semi-metallic. Here, the spin up bands slightly cross the Fermi level (around Γ) as compared to the spin down bands. In the spin up channel, the band splits from Γ point below the Fermi level and reconstructs at other Γ point. Interestingly, these split band forms gapped type of Dirac cone at K point above the Fermi level in the spin up channel. The situation of band splitting for spin down channel is the same as that of the spin up channel.

To describe the electronic band structure of Mn doped Ti_2NO_2, we divided the bands into separate sub-bands (i.e A, B, C, D, and E) in the spin up channel and three sub-bands (i.e A, B, and C) in the spin down channel, respectively. The conduction bands are significantly dominated by Ti-3d states and trivially contributed from other states. The sub-bands B and C are dominated by Mn-3d states. In the spin up channel, the sub-bands A and B form indirect energy gap of 0.52 eV. Similarly, the energy gaps between sub-bands B and C, and C and D are 0.62 eV (direct) and 0.19 eV (indirect), respectively. The sub-bands D and E are significantly concentrated from the O-2p states along with Ti-3d and Mn-3d states. In the case of spin down channel, the energy gap between sub-bands A and B is 1.71 eV (direct). The same behavior is seen in sub-bands B and C.

Here, the asymmetrical nature of the PDOS corresponding to the spin up and spin down channels give

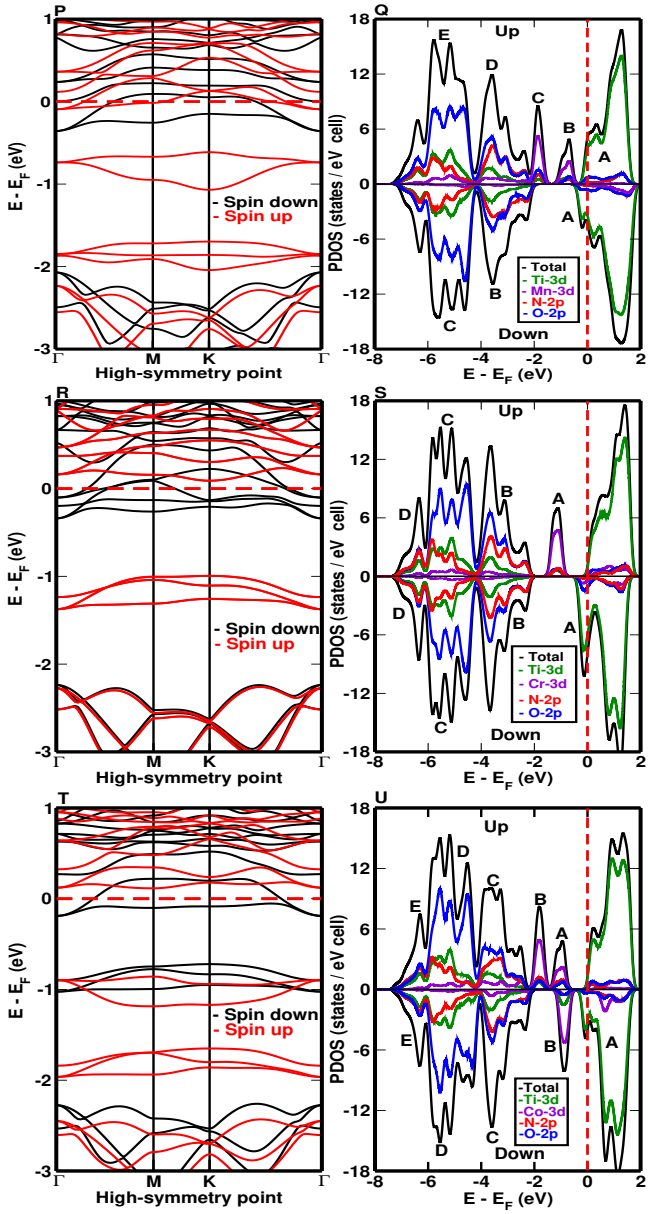

FIG. 21. (Color online) P-Q, R-S, and T-U represent the electronic band structures and PDOS of Mn, Cr, and Co doped Ti_2NO_2 MXene. The half-metallic behaviors are clearly seen in the band structures. The unphysical DOS appeared in the spin up channels with gaussian smearing are mitigated by tetrahedron integration method (shown in FIGs. 22 and 23). The red dashed lines indicate the position of the Fermi level.

rise to ferromagnetism (3.98 μ_B per cell) preserving the weak semi- metallic nature, which originates from the 3d states of Mn and Ti atoms. The intrinsic magnetic moment of Mn is 3.73 μ_B when it is dopped on the top layer of Ti_2NO_2. This doping reduces the magnetic moment of Ti from 0.28 μ_B to smaller but non negligible values.

In contrast to Mn doped system, the spin up channel shows the semi-conducting nature with direct band gaps of 1.07 eV (at K point) and 0.97 eV (at M point) for

Cr and Co, respectively. The 3d electrons of TM are responsible for the semi-conducting behavior in both doped systems. In the spin down channel, the bands cross the Fermi level representing the metallic character. Thus, the semi-conducting nature in the spin up channel and metallic nature in the spin down channel predict the half-metallic character in both Cr and Co doped systems with 100% spin polarization.

For Cr dopped system (FIG. 21S), the bands above the Fermi level are mostly dominated by Ti-3d with smaller contributions from Cr-3d, O-2p, and N-2p. To describe valence states, we divided it into four different sub-bands A, B, C, and D. The sub-band A is dominated by Cr-3d states in the spin up channel and by Ti-3d states in the spin down channel. The direct energy gaps between the sub-bands A and B are 1.90 eV and 0.91 eV for the spin down and spin up channels, respectively. The sub-bands B, C, and D are the mixed states with major contribution from the O-2p states.

Similarly, the PDOS of Co doped system is shown in FIG. 21U. In the unoccupied states, the bands are dominated by Ti-3d states. Coincidentally, two energy gaps are found toward the occupied states in both spin channels. In spin up channel, the sub-bands A and B are mainly dominated by Co-3d states forming an indirect energy gap of 0.47 eV. The energy gap between B and C forms indirect gap of 0.47 eV. In spin down channel, the sub-bands A and B are mainly dominated by Ti-3d and Co-3d states, respectively. The indirect energy gaps between sub-bands A and B, and B and C are of 0.5 eV and 1.34 eV, respectively. In both channels, the sub-bands C, D, and E show the major contribution from O-2p states along with N-2p, Ti-3d, and Mn-3d states.

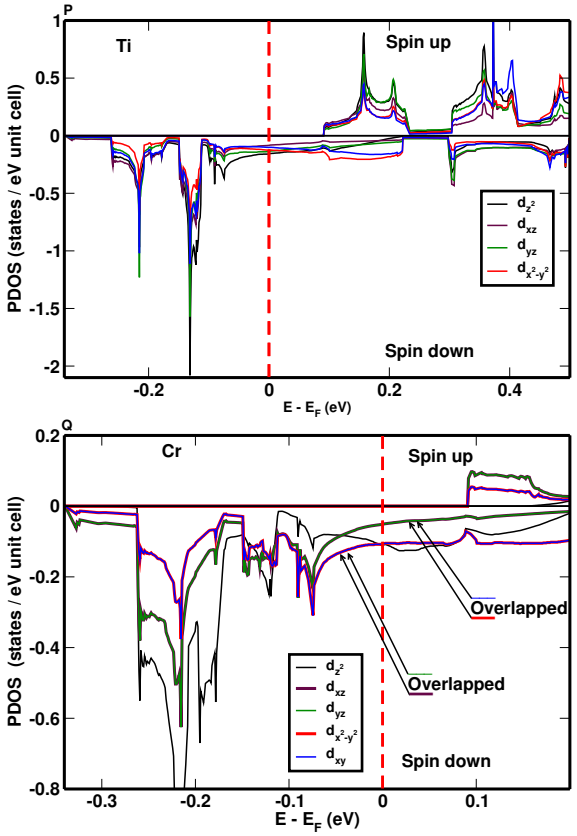

FIG. 22. (Color online) P and Q represent the projected spin polarized 3d DOS of Ti and Cr (with tetrahedron method) following octahedral phase with D_{3d} point group corresponding to t_{2g} (d_{xz}, d_{yz}, and d_{xy}) and e_g ($d_{x^2-y^2}$ and d_{z^2}) states in Cr doped Ti_2NO_2. The red dashed lines represent the position of the Fermi level.

Origin of Half-metallic Gap in Cr and Co Doped Ti_2NO_2

The 3d electrons of Cr and Co play a significant role for half-metallicity and magnetism. Figure 22 (P and Q) represents the projected spin polarized 3d DOS of Ti and Cr, respectively. The substitution of Cr allows to transform from the half-metallic FM to the half-metallic AFM. The half-metallicity is originated from both 3d electrons of Ti and Cr atoms. Unlike doped free phase, the Cr substitution changes the positive exchange to negative exchange splitting (spin up - spin down) with energy of 0.42 eV. The Cr substitution allows all the components of t_{2g} states (d_{xz}, d_{yz}, and d_{xy}) and e_g ($d_{x^2-y^2}$ and d_{z^2}) states of Ti to be non-degenerate states, whereas $d_{x^2-y^2}$ of e_g and d_{xy} of t_{2g}, and d_{xz} and d_{yz} of t_{2g} states are degenerate in the case of Cr. The d_{z^2} state also shows the dominant nature in both Ti and Cr atoms. In Cr doped case, there are two possibilities to fill the non-bonding states. Presuming all the constituents of Ti_2NO_2 are in their normal oxidation states, the top and bottom Ti atoms have either +4 or +3 oxidation states as mentioned above. Similarly, the top of Cr and the bottom of Ti have either +4 or +3 oxidation states after providing two electrons to O and three electrons to N atom. Following Hund's rule, the remaining 3d electrons of Ti and Cr fill partially the non-bonding states. These free 3d electrons in non-bonding states give AFM character. The individual magnetic moments of Ti and Cr align anti-parallely. The Cr moment here is one order magnitude larger than those of Ti atoms. Furthermore, the individual magnetic moments of Cr and Ti split the non-boding states into fully occupied bands in the spin down channel and open band gap in the spin up channel revealing the semi-conducting behavior.

Similarly, Co substitution also preserves the FM half-metallic character with total magnetization of 1.05 μ_B (FIG. 23). The magnetic moment of Co in Ti_2NO_2 is 1.90 μ_B, which diminishes the individual magnetic moments of Ti from 0.28 μ_B to smaller but non negligible values. The spin alignment of Co is anti-parallel with all Ti atoms except for one Ti in the bottom layer making the system overall FM. The Co substitution also favors the negative exchange splitting with energy 0.16 eV. Similarly, this substitution allows all the components of t_{2g}

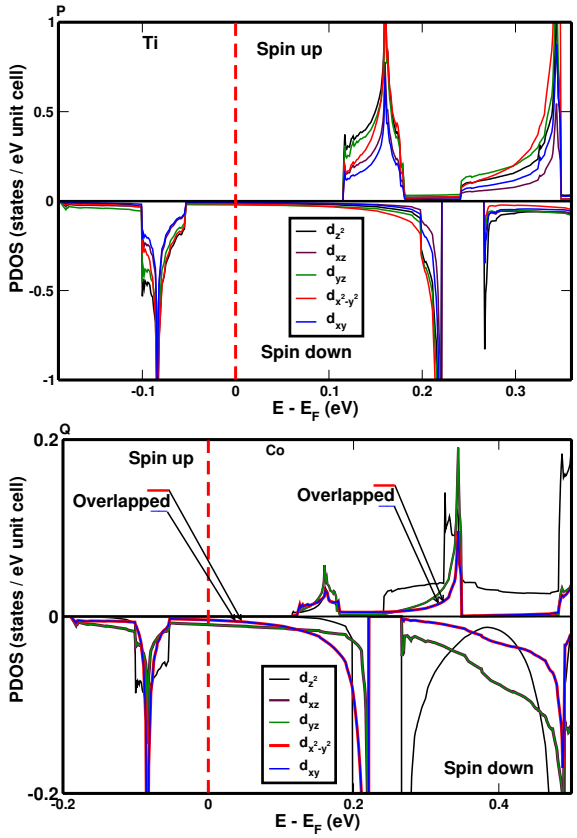

FIG. 23. (Color online) P and Q represent the projected spin polarized $3d$ DOS of Ti and Co (with tetrahedron method) following octahedral phase with D_{3d} point group corresponding to t_{2g} (d_{xz}, d_{yz}, and d_{xy}) and e_g ($d_{x^2-y^2}$ and d_{z^2}) states in Co doped Ti_2NO_2. The red dashed lines represent the position of the Fermi level.

(d_{xz}, d_{yz}, and d_{xy}) and e_g ($d_{x^2-y^2}$ and d_{z^2}) states of Ti to be non-degenerate states, whereas $d_{x^2-y^2}$ of e_g and d_{xy} of t_{2g}, and d_{xz} and d_{yz} of t_{2g} states are degenerate states in the case of Co (FIG. 23P and 23Q). The d_{z^2} state also shows the dominant character in both Ti and Co.

Conclusion

In summary, we have systematically studied the structural, electronic band structure, and magnetic properties of MAX phase Ti_2AlN, bare MXene Ti_2N, and functionalized MXenes Ti_2NT_2 (T= -OH, -H, -O, -F). The formation and cohesive energies favor the chemical and structural stabilities in all MXenes and parent MAX phase, however, Ti_2NO_2 and Ti_2NF_2 are apparently more stable than others. Furthermore, the well separated optical and acoustic branches with no imaginary phonon frequency reveals the dynamical stability of Ti_2N. The bare MXene is FM but after surface termination, the ferromagnetism is completely removed except for -O termination (Ti_2NO_2), which is half-metallic FM. The companionship of SOC strongly influences the bare MXene by spliting and forming Dirac topological features, and coupling opposite spin channels to form band inversion. This band inversion is caused by both time reversal symmetry breaking and hybridization of different spin components of t_{2g} and e_g states of Ti-$3d$.

The strain significantly influences the Fermi level with peculiar band crossings. The Fermi level shifts toward the lower energy states under compression and it shifts toward the higher energy states under tensile strain in Ti_2NH_2. These features are reversed in the case of Ti_2N, Ti_2NF_2, and $Ti_2N(OH)_2$. The Ti_2NO_2 exhibits exotic electronic structure and magnetic states not only in pristine but also in strained and defected structures. Its 100% spin polarized half-metallic FM characteristic changes to weakly half-metallic under 1% compression and it is completely destroyed in 2% compression. The Ti defect in this material changes the electronic properties from half-metal to semi-conductor, whereas O defect changes to semi-metallic. In the N defect, the material changes from half-metallic characteristic to the metallic characteristic. The variable vacancy concentration allows to change the weak semi-conductor to strong semi-conductor. The 12.5% Co substitution preserves the half-metallic character, whereas Mn substitution changes the electronic properties from the half-metallic to weak semi-metallic preserving the FM character. However, Cr substitution changes the magnetic properties from FM to AFM preserving the half-metallicity. The magnetism and half-metallicity are mainly due to different orbital filling configurations of $3d$ electrons of transition metals. The presence of the half-metallicity in pristine, and Cr and Co substitutions in Ti_2NO_2 could provide magnetic functionalities in spintronic applications.

ACKNOWLEDGMENTS

The predictive understanding, specific to electronic (band) structure, magnetism, defect, and strain induced effects, made in this work were developed by D. P. and his group in the Critical Materials Institute, an Energy Innovation Hub led by the Ames Laboratory and funded by the U. S. Department of Energy, Office of Energy Efficiency and Renewable Energy, Advanced Manufacturing Office. D. P. would like to acknowledge Ed Moxley for maintaining computational facilities, including the RAMAN cluster and computational software. N. K. S. would like to acknowledge UGC Nepal for partial financial support.

* gopi.kaphle@cdp.tu.edu.np, gck223@gmail.com

[1] K. S Novoselov, A. K Geim, S. V Morozov, D. Jiang, Y. Zhang, S. V Dubonos, I. V Grigorieva, and A. A Firsov, "*Electric field effect in atomically thin carbon films*," science **306**, 666–669 (2004).

[2] R. Mas-Balleste, C. Gomez-Navarro, J. Gomez-Herrero, and F. Zamora, "*2D materials: to graphene and beyond*," Nanoscale **3**, 20–30 (2011).

[3] M. J. Allen, V. C. Tung, and R. B. Kaner, "*Honeycomb carbon: a review of graphene*," Chem. Rev. **110**, 132–145 (2010).

[4] C. Tan, X. Cao, X. J. Wu, Q. He, J. Yang, X. Zhang, J. Chen, W. Zhao, S. Han, G. H. Nam, *et al.*, "*Recent advances in ultrathin two-dimensional nanomaterials*," Chem. Rev. **117**, 6225–6331 (2017).

[5] Q. Jiang, N. Kurra, M. Alhabeb, Y. Gogotsi, and H. N. Alshareef, "*All pseudocapacitive MXene-RuO_2 asymmetric supercapacitors*," Adv. Energy Mater. **8**, 1703043 (2018).

[6] N. K. Chaudhari, H. Jin, B. Kim, D. San Baek, S. H. Joo, and K. Lee, "*MXene: an emerging two-dimensional material for future energy conversion and storage applications*," J. Mater. Chem. A **5**, 24564–24579 (2017).

[7] K. Huang, Z. Li, J. Lin, G. Han, and P. Huang, "*Two-dimensional transition metal carbides and nitrides (MXenes) for biomedical applications*," Chem. Soc. Rev. **47**, 5109–5124 (2018).

[8] A. Sinha, H. Zhao, Y. Huang, X. Lu, J. Chen, R. Jain, *et al.*, "*MXene: An emerging material for sensing and biosensing*," Trends Analyt Chem **105**, 424–435 (2018).

[9] X. Li, C. Wang, Y. Cao, and G. Wang, "*Functional MXene materials: progress of their applications*," Chem.: Asian J. **13**, 2742–2757 (2018).

[10] H. Kumar, N. C. Frey, L. Dong, B. Anasori, Y. Gogotsi, and V. B. Shenoy, "*Tunable magnetism and transport properties in nitride MXenes*," ACS nano **11**, 7648–7655 (2017).

[11] B. Anasori, M. R. Lukatskaya, and Y. Gogotsi, "*2D metal carbides and nitrides (MXenes) for energy storage*," Nat. Rev. Mater. **2**, 1–17 (2017).

[12] M. Magnuson, O. Wilhelmsson, J. P. Palmquist, U. Jansson, M. Mattesini, S. Li, R. Ahuja, and O. Eriksson, "*Electronic structure and chemical bonding in Ti_2AlC investigated by soft x-ray emission spectroscopy*," Phys. Rev. B **74**, 195108 (2006).

[13] M. W. Barsoum and M. Radovic, "*Elastic and mechanical properties of the MAX phases*," Annu. Rev. Mater. Sci. **41**, 195–227 (2011).

[14] N. C. Osti, M. Naguib, A. Ostadhossein, Y. Xie, P. R. C. Kent, B. Dyatkin, G. Rother, W. T. Heller, A. C. T. Van Duin, Y. Gogotsi, *et al.*, "*Effect of metal ion intercalation on the structure of MXene and water dynamics on its internal surfaces*," ACS Appl. Mater. Interfaces **8**, 8859–8863 (2016).

[15] M. Ghidiu, S. Kota, J. Halim, A. W. Sherwood, N. Nedfors, J. Rosen, V. N. Mochalin, and M. W. Barsoum, "*Alkylammonium cation intercalation into Ti_3C_2 (MXene): Effects on properties and ion-exchange capacity estimation*," Chem. Mater. **29**, 1099–1106 (2017).

[16] A. Lipatov, M. Alhabeb, M. R. Lukatskaya, A. Boson, Y. Gogotsi, and A. Sinitskii, "*Effect of synthesis on quality, electronic properties and environmental stability of individual monolayer Ti3C2 MXene flakes*," Adv. Electron. Mater. **2**, 1600255 (2016).

[17] B. Soundiraraju and B. K. George, "*Two-dimensional titanium nitride (Ti_2N) MXene: synthesis, characterization, and potential application as surface-enhanced Raman scattering substrate*," ACS nano **11**, 8892–8900 (2017).

[18] P. Urbankowski, B. Anasori, T. Makaryan, D. Er, S. Kota, P. L. Walsh, M. Zhao, V. B. Shenoy, M. W. Barsoum, and Y. Gogotsi, "*Synthesis of two-dimensional titanium nitride Ti_4N_3 (MXene)*," Nanoscale **8**, 11385–11391 (2016).

[19] Y. Xie and P. R. C. Kent, "*Hybrid density functional study of structural and electronic properties of functionalized $Ti_{n+1}X_n$ (X= C, N) monolayers*," Phys. Rev. B **87**, 235441 (2013).

[20] C. Zhan, W. Sun, P. R. C. Kent, M. Naguib, Y. Gogotsi, and D. Jiang, "*Computational screening of MXene electrodes for pseudocapacitive energy storage*," J. Phys. Chem. C **123**, 315–321 (2018).

[21] K. Hantanasirisakul and Y. Gogotsi, "*Electronic and optical properties of 2D transition metal carbides and nitrides (MXenes)*," Adv. Mater. **30**, 1804779 (2018).

[22] S. Postorino, D. Grassano, M. D′Alessandro, A. Pianetti, O. Pulci, and M. Palummo, "*Strain-induced effects on the electronic properties of 2D materials*," Nanomater. Nanotechnol. **10**, 1847980420902569 (2020).

[23] M. Sharma, A. Kumar, P. K. Ahluwalia, and R. Pandey, "*Strain and electric field induced electronic properties of two-dimensional hybrid bilayers of transition-metal dichalcogenides*," J. Appl. Phys. **116**, 063711 (2014).

[24] C. Lee, X. Wei, J. W. Kysar, and J. Hone, "*Measurement of the elastic properties and intrinsic strength of monolayer graphene*," science **321**, 385–388 (2008).

[25] Y. Li, N. Li, S. Zhao, J. Fan, and J. J. Kai, "*Strain-tunable electronic properties and lithium storage of 2D transition metal carbide (MXene) Ti_2CO_2 as a flexible electrode*," J. Mater. Chem. A **8**, 760–769 (2020).

[26] A. Bandyopadhyay, D. Ghosh, and S. K. Pati, "*Effects of point defects on the magnetoelectronic structures of MXenes from first principles*," Phys. Chem. Chem. Phys. **20**, 4012–4019 (2018).

[27] X. Sang, Y. Xie, M. W. Lin, M. Alhabeb, K. L. Van Aken, Y. Gogotsi, P. R. C. Kent, K. Xiao, and R. R. Unocic, "*Atomic Defects in Monolayer Titanium Carbide ($Ti_3C_2T_x$) MXene*," ACS nano **10**, 9193–9200 (2016).

[28] R. Liu, W. Cao, D. Han, Y. Mo, H. Zeng, H. Yang, and W. Li, "*Nitrogen-doped Nb_2CT_x MXene as anode materials for lithium ion batteries*," J. Alloys Compd. **793**, 505–511 (2019).

[29] C. F. Du, X. Sun, H. Yu, Q. Liang, K. N. Dinh, Y. Zheng, Y. Luo, Z. Wang, and Q. Yan, "*Synergy of Nb doping and surface alloy enhanced on water–alkali electrocatalytic hydrogen generation performance in Ti-based MXene*," Adv. Sci. **6**, 1900116 (2019).

[30] P. Chakraborty, T. Das, D. Nafday, L. Boeri, and T. Saha-Dasgupta, "*Manipulating the mechanical properties of Ti_2C MXene: Effect of substitutional doping*," Phys. Rev. B **95**, 184106 (2017).

[31] L. C. Xu, R. Z. Wang, M. S. Miao, X. L. Wei, Y. P. Chen, H. Yan, W. M. Lau, L. M. Liu, and Y. M. Ma, "*Two dimensional Dirac carbon allotropes from graphene*," Nanoscale **6**, 1113–1118 (2014).

[32] D. Malko, C. Neiss, F. Vines, and A. Görling, "*Competition for graphene: graphynes with direction-dependent dirac cones*," Phys. Rev. Lett. **108**, 086804 (2012).

[33] N. Tajima, "*Effects of carrier doping on the transport in the Dirac electron system α-(BEDT-TTF) 2I3 under high pressure*," Crystals **8**, 126 (2018).

[34] Y. Zhang, Y. W. Tan, H. L. Stormer, and P. Kim, "*Experimental observation of the quantum Hall effect and*

Berry's phase in graphene," nature **438**, 201–204 (2005).

[35] F. Islam, R. Choudhary, Y. Liu, B. G. Ueland, D. Paudyal, T. Heitmann, R. J. McQueeney, and D. Vaknin, "*Controlling magnetic order, magnetic anisotropy, and band topology in the semimetals Sr (Mn 0.9 Cu 0.1) Sb_2 and Sr (Mn 0.9 Zn 0.1) Sb_2*," Phys. Rev. B **102**, 085130 (2020).

[36] X. Shao, X. Liu, X. Zhang, J. Wang, and M. Zhao, "*Zr_2Si: an antiferromagnetic Dirac MXene*," Phys. Chem. Chem. Phys. **20**, 3946–3952 (2018).

[37] H. Fashandi, V. Ivády, P. Eklund, A. L. Spetz, M. I. Katsnelson, and I. A. Abrikosov, "*Dirac points with giant spin-orbit splitting in the electronic structure of two-dimensional transition-metal carbides*," Phys. Rev. B **92**, 155142 (2015).

[38] P. Giannozzi, O. Baseggio, P. Bonfà, D. Brunato, R. Car, I. Carnimeo, C. Cavazzoni, S. de Gironcoli, P. Delugas, F. Ferrari Ruffino, A. Ferretti, N. Marzari, I. Timrov, A. Urru, and S. Baroni, "*Quantum ESPRESSO toward the exascale*," J. Chem. Phys. **152**, 154105 (2020).

[39] P. Giannozzi, S. Baroni, N. Bonini, M. Calandra, R. Car, C. Cavazzoni, D. Ceresoli, G. L. Chiarotti, M. Cococcioni, I. Dabo, A. D. Corso, S. d. Gironcoli, S. Fabris, G. Fratesi, R. Gebauer, U. Gerstmann, C. Gougoussis, A. Kokalj, M. Lazzeri, L. Martin-Samos, N. Marzari, F. Mauri, R. Mazzarello, S. Paolini, A. Pasquarello, L. Paulatto, C. Sbraccia, S. Scandolo, G. Sclauzero, A. P. Seitsonen, A. Smogunov, P. Umari, and R. M. Wentzcovitch, "*QUANTUM ESPRESSO: a modular and open-source software project for quantum simulations of materials*," J. Phys.: Condens. Matter **21**, 395502 (2009).

[40] J. P. Perdew, K. Burke, and M. Ernzerhof, "*Generalized gradient approximation made simple*," Phys. Rev. Lett. **77**, 3865 (1996).

[41] S. Grimme, "*Semiempirical GGA-type density functional constructed with a long-range dispersion correction*," J. Comput. Chem. **27**, 1787–1799 (2006).

[42] A. H. MacDonald and S. H. Vosko, "*A relativistic density functional formalism*," J. Phys. C: Solid State Phys. **12**, 2977–2990 (1979).

[43] Y. S. Lee, W. C. Ermler, and K. S. Pitzer, "*Ab initio effective core potentials including relativistic effects.: I. Formalism and applications to the Xe and Au atoms*," in *Molecular Structure And Statistical Thermodynamics: Selected Papers of Kenneth S Pitzer* (World Scientific, 1993) pp. 112–127.

[44] W. Kohn and L. J. Sham, "*Self-consistent equations including exchange and correlation effects*," Phys. Rev. **140**, A1133 (1965).

[45] A. Dal Corso, "*Projector augmented wave method with spin-orbit coupling: Applications to simple solids and zincblende-type semiconductors*," Phys. Rev. B **86**, 085135 (2012).

[46] R. Cuadrado and J. Cerdá, "*Fully relativistic pseudopotential formalism under an atomic orbital basis: Spin–orbit splittings and magnetic anisotropies*," J. Condens. Matter Phys. **24**, 086005 (2012).

[47] P. E. Blöchl, "*Projector augmented-wave method*," Phys. Rev. B **50**, 17953 (1994).

[48] P. V. Medeiros, S. Stafström, and J. Björk, "*Effects of extrinsic and intrinsic perturbations on the electronic structure of graphene: Retaining an effective primitive cell band structure by band unfolding*," Phys. Rev. B **89**, 041407 (2014).

[49] V. Popescu and A. Zunger, "*Extracting E versus k effective band structure from supercell calculations on alloys and impurities*," Phys. Rev. B **85**, 085201 (2012).

[50] D. Dombrowski, W. Jolie, M. Petrović, S. Runte, F. Craes, J. Klinkhammer, M. Kralj, P. Lazić, E. Sela, and C. Busse, "*Energy-dependent chirality effects in quasifree-standing graphene*," Phys. Rev. Lett. **118**, 116401 (2017).

[51] J. Warmuth, A. Bruix, M. Michiardi, T. Hänke, M. Bianchi, J. Wiebe, R. Wiesendanger, B. Hammer, P. Hofmann, and A. A. Khajetoorians, "*Band-gap engineering by Bi intercalation of graphene on Ir (111)*," Phys. Rev. B **93**, 165437 (2016).

[52] X. Cartoixà, M. Palummo, H. I. T. Hauge, E. P. Bakkers, and R. Rurali, "*Optical emission in hexagonal SiGe nanowires*," Nano Lett. **17**, 4753–4758 (2017).

[53] R. M. Ronchi, J. T. Arantes, and S. F. Santos, "*Synthesis, structure, properties and applications of MXenes: Current status and perspectives*," Ceram. Int. **45**, 18167–18188 (2019).

[54] A. Szuplewska, A. Rozmysłowska-Wojciechowska, S. Poźniak, T. Wojciechowski, M. Birowska, M. Popielski, M. Chudy, W. Ziemkowska, L. Chlubny, D. Moszczyńska, *et al.*, "*Multilayered stable 2D nano-sheets of Ti_2NT_x MXene: synthesis, characterization, and anticancer activity*," J. Nanobiotechnology **17**, 1–14 (2019).

[55] H. Tang, W. Li, L. Pan, K. Tu, F. Du, T. Qiu, J. Yang, C. P. Cullen, N. McEvoy, and C. Zhang, "*A Robust, Freestanding MXene-Sulfur Conductive Paper for Long-Lifetime Li–S Batteries*," Adv. Funct. Mater. **29**, 1901907 (2019).

[56] J. L. Hart, K. Hantanasirisakul, A. C. Lang, B. Anasori, D. Pinto, Y. Pivak, J. T. van Omme, S. J. May, Y. Gogotsi, and M. L. Taheri, "*Control of MXenes' electronic properties through termination and intercalation*," Nat. Commun. **10**, 1–10 (2019).

[57] M. Naguib, V. N. Mochalin, M. W. Barsoum, and Y. Gogotsi, "*25th anniversary article: MXenes: a new family of two-dimensional materials*," Adv. Mater. **26**, 992–1005 (2014).

[58] V. M. H. Ng, H. Huang, K. Zhou, P. S. Lee, W. Que, J. Z. Xu, and L. B. Kong, "*Recent progress in layered transition metal carbides and/or nitrides (MXenes) and their composites: synthesis and applications*," J. Mater. Chem. A **5**, 3039–3068 (2017).

[59] M. Naguib, M. Kurtoglu, V. Presser, J. Lu, J. Niu, M. Heon, L. Hultman, Y. Gogotsi, and M. W. Barsoum, "*Two-dimensional nanocrystals produced by exfoliation of Ti_3AlC_2*," Adv. Mater. **23**, 4248–4253 (2011).

[60] M. Khazaei, M. Arai, T. Sasaki, C. Y. Chung, N. S. Venkataramanan, M. Estili, Y. Sakka, and Y. Kawazoe, "*Novel electronic and magnetic properties of two-dimensional transition metal carbides and nitrides*," Adv. Funct. Mater. **23**, 2185–2192 (2013).

[61] D. Wang, Y. Gao, Y. Liu, D. Jin, Y. Gogotsi, X. Meng, F. Du, G. Chen, and Y. Wei, "*First-principles calculations of Ti_2N and Ti_2NT_2 (T= O, F, OH) monolayers as potential anode materials for lithium-ion batteries and beyond*," J. Phys. Chem. C **121**, 13025–13034 (2017).

[62] X. Wang, Z. Cheng, J. Wang, L. Wang, Z. Yu, C. Fang, J. Yang, and G. Liu, "*Origin of the half-metallic band-gap in newly designed quaternary Heusler compounds ZrVTiZ (Z= Al, Ga)*," RSC Adv. **6**, 57041–57047 (2016).

[63] G. Gao, G. Ding, J. Li, K. Yao, M. Wu, and M. Qian, "*Monolayer MXenes: promising half-metals and spin gapless semiconductors*," Nanoscale **8**, 8986–8994 (2016).

[64] N. Zhang, Y. Hong, S. Yazdanparast, and M. A. Zaeem, "*Superior structural, elastic and electronic properties of 2D titanium nitride MXenes over carbide MXenes: a comprehensive first principles study*," 2D Mater. **5**, 045004 (2018).

[65] J. E. Saal, S. Kirklin, M. Aykol, B. Meredig, and C. Wolverton, "*Materials design and discovery with high-throughput density functional theory: the open quantum materials database (OQMD)*," Jom **65**, 1501–1509 (2013).

[66] S. Kirklin, J. E. Saal, B. Meredig, A. Thompson, J. W. Doak, M. Aykol, S. Rühl, and C. Wolverton, "*The Open Quantum Materials Database (OQMD): assessing the accuracy of DFT formation energies*," Npj Comput. Mater. **1**, 1–15 (2015).

[67] P. M. Kowalski, M. F. Camellone, N. N Nair, B. Meyer, and D. Marx, "*Charge localization dynamics induced by oxygen vacancies on the TiO_2 (110) surface*," Phys. Rev. Lett. **105**, 146405 (2010).

[68] E. Tisserond, J. Fuchs, M. Goerbig, P. Auban-Senzier, C. Mézière, P. Batail, Y. Kawasugi, M. Suda, H. Yamamoto, R. Kato, *et al.*, "*Aperiodic quantum oscillations of particle-hole asymmetric Dirac cones*," EPL (Europhysics Letters) **119**, 67001 (2017).

[69] G. Chang, B. Singh, S. Y. Xu, G. Bian, S. M. Huang, C. H. Hsu, I. Belopolski, N. Alidoust, D. S. Sanchez, H. Zheng, *et al.*, "*Magnetic and noncentrosymmetric Weyl fermion semimetals in the RAlGe family of compounds (R= rare earth)*," Phys. Rev. B **97**, 041104 (2018).

[70] F. Guillou, D. Paudyal, Y. Mudryk, A. K. Pathak, V. Smetana, A. V. Mudring, and V. K. Pecharsky, "*Metamagnetic transition, magnetocaloric effect and electronic structure of the rare-earth anti-perovskite $SnOEu_3$*," J. Magn. Magn. Mater. **501**, 166405 (2020).

[71] Y. Zhang, K. He, C. Z. Chang, C. L. Song, L. L Wang, X. Chen, J. F. Jia, Z. Fang, X. Dai, W. Y. Shan, *et al.*, "*Crossover of the three-dimensional topological insulator Bi_2Se_3 to the two-dimensional limit*," Nat. Phys. **6**, 584–588 (2010).

[72] J. K. Desmarais, J. P. Flament, and A. Erba, "*Spin-orbit coupling in periodic systems with broken time-reversal symmetry: Formal and computational aspects*," Phys. Rev. B **101**, 235142 (2020).

[73] S. Souma, M. Komatsu, M. Nomura, T. Sato, A. Takayama, T. Takahashi, K. Eto, K. Segawa, and Y. Ando, "*Spin polarization of gapped Dirac surface states near the topological phase transition in TlBi $(S_{1-x}Se_x)_2$*," Phys. Rev. Lett. **109**, 186804 (2012).

[74] H. Ji, I. Pletikosić, Q. D. Gibson, G. Sahasrabudhe, T. Valla, and R. J. Cava, "*Strong topological metal material with multiple Dirac cones*," Phys. Rev. B **93**, 045315 (2016).

[75] N. Kodama, M. Yamaga, and B. Henderson, "*Energy levels and symmetry of Ce^{3+} in fluoride and oxide crystals*," J. Appl. Phys. **84**, 5820–5822 (1998).

[76] Y. M. Xie, B. T. Zhou, and K. T. Law, "*Spin-Orbit-Parity-Coupled Superconductivity in Topological Monolayer WTe_2*," Phys. Rev. Lett. **125**, 107001 (2020).

[77] Q. Gao and H. Zhang, "*Magnetic i-MXenes: a new class of multifunctional two-dimensional materials*," Nanoscale **12**, 5995–6001 (2020).

[78] M. Zeng, C. Fang, G. Chang, Y. A. Chen, T. Hsieh, A. Bansil, H. Lin, and L. Fu, "*Topological semimetals and topological insulators in rare earth monopnictides*," arXiv preprint arXiv:1504.03492 (2015).

[79] S. Nie, H. Weng, and F. B. Prinz, "*Topological nodal-line semimetals in ferromagnetic rare-earth-metal monohalides*," Phys. Rev. B **99**, 035125 (2019).

[80] S. Tang, C. Zhang, D. Wong, Z. Pedramrazi, H. Z. Tsai, C. Jia, B. Moritz, M. Claassen, H. Ryu, S. Kahn, *et al.*, "*Quantum spin Hall state in monolayer 1T'-WTe_2*," Nat. Phys. **13**, 683–687 (2017).

[81] C. Si, K. H. Jin, J. Zhou, Z. Sun, and F. Liu, "*Large-gap quantum spin Hall state in MXenes: d-band topological order in a triangular lattice*," Nano Lett. **16**, 6584–6591 (2016).

[82] S. Li, W. x. Ji, S. J Hu, C. W Zhang, and S. S Yan, "*Effect of amidogen functionalization on quantum spin Hall effect in Bi/Sb (111) films*," ACS Appl. Mater. Interfaces **9**, 41443–41453 (2017).

[83] H. Sun, S. S. Li, W. X Ji, and C. W. Zhang, "*Valley-dependent topological phase transition and quantum anomalous valley Hall effect in single-layer RuClBr*," Phys. Rev. B **105**, 195112 (2022).

[84] S. Chege, P. Ning'i, J. Sifuna, and G. O. Amolo, "*Origin of band inversion in topological Bi_2Se_3*," AIP Adv. **10**, 095018 (2020).

[85] X. Wang and T. Zhou, "*Fragile topology in nodal-line semimetal superconductors with double band inversion*," arXiv preprint arXiv:2106.06928 (2021).

[86] W. Ku, T. Berlijn, C. C. Lee, *et al.*, "*Unfolding first-principles band structures*," Phys. Rev. Lett. **104**, 216401 (2010).

[87] Y. Zhou and Z. Sun, "*Electronic structure and bonding properties of layered machinable Ti_2AlC and Ti_2AlN ceramics*," Phys. Rev. B **61**, 12570 (2000).

[88] G. Hug and E. Fries, "*Full-potential electronic structure of Ti_2AlC and Ti_2AlN*," Phys. Rev. B **65**, 113104 (2002).

[89] L. Petit, D. Paudyal, Y. Mudryk, K. A. Gschneidner Jr, V. K. Pecharsky, M. Lüders, Z. Szotek, R. Banerjee, and J. B. Staunton, "*Complex magnetism of lanthanide intermetallics and the role of their valence electrons: Ab initio theory and experiment*," Phys. Rev. Lett. **115**, 207201 (2015).

[90] M. Chhowalla, H. S. Shin, G. Eda, L. J. Li, K. P. Loh, and H. Zhang, "*The chemistry of two-dimensional layered transition metal dichalcogenide nanosheets*," Nat. Chem **5**, 263–275 (2013).

[91] M. Khazaei, A. Ranjbar, M. Arai, and S. Yunoki, "*Topological insulators in the ordered double transition metals M_2MC_2 MXenes (M= Mo, W; M = Ti, Zr, Hf)*," Phys. Rev. B **94**, 125152 (2016).

[92] M. I. Katsnelson, V. Y. Irkhin, L. Chioncel, A. I. Lichtenstein, and R. A. de Groot, "*Half-metallic ferromagnets: From band structure to many-body effects*," Rev. Mod. Phys. **80**, 315 (2008).

[93] X. Li and J. Yang, "*First-principles design of spintronics materials*," Natl. Sci. Rev. **3**, 365–381 (2016).

[94] S. S. Yu, W. T. Zheng, Q. B. Wen, and Q. Jiang, "*First principle calculations of the electronic properties of nitrogen-doped carbon nanoribbons with zigzag edges*," Carbon **46**, 537–543 (2008).

[95] Y. J. Liu, B. Gao, D. Xu, H. M. Wang, and J. X. Zhao, "*Theoretical study on Si-doped hexagonal boron nitride*

(h-BN) sheet: Electronic, magnetic properties, and reactivity," Phys. Lett. A **378**, 2989–2994 (2014).